npj | computational materials

Article

Published in partnership with the Shanghai Institute of Ceramics of the Chinese Academy of Sciences

https://doi.org/10.1038/s41524-026-02026-9

# Extraction of the self energy and Eliashberg function from angle resolved photoemission spectroscopy using the xARPES code



Thomas P. van Waas[1] ✉, Christophe Berthod[2], Jan Berges[3], Nicola Marzari[3,4,5], J. Hugo Dil[6,7] & Samuel Poncé[1,8] ✉

Angle-resolved photoemission spectroscopy is a powerful experimental technique for studying anisotropic many-body interactions through the electron spectral function. Existing attempts to decompose the spectral function into non-interacting dispersions and electron-phonon, electron-electron, and electron-impurity self-energies rely on linearization of the bands and manual assignment of self-energy magnitudes. Here, we show how self-energies can be extracted consistently for curved dispersions. We extend the maximum-entropy method to Eliashberg-function extraction with Bayesian inference, optimizing the parameters describing the dispersions and the magnitudes of electron-electron and electron-impurity interactions. We compare these novel methodologies with state-of-the-art approaches on model data, then demonstrate their applicability with two high-quality experimental data sets. With the first set, we identify the phonon modes of a two-dimensional electron liquid on $TiO_2$-terminated $SrTiO_3$. With the second set, we obtain unprecedented agreement between two Eliashberg functions of Li-doped graphene extracted from separate dispersions. We release these functionalities in the novel Python code xARPES.

The coupling of electrons with bosons is a central subject in condensed matter physics[1], governing many experimental phenomena[1–6]. In solids, a commonly encountered boson is the phonon, where lattice vibrations affect electronic properties such as the resistivity in metals[7], Cooper pairing in conventional superconductors[8], lifetimes of electron spins[9], and the formation of polarons[10]. Depending on the material, the coupling of electrons with other types of bosons such as magnons[11,12] and plasmons[13] may also show pronounced effects. In this work, we focus on systems where electron-phonon coupling (EPC) is the predominant type of electron-boson coupling, as it is intrinsic to all materials. In metals, EPC typically appears as a photoemission kink in the spectral function near the chemical potential[14], which can be quantified in terms of the Eliashberg function[15]. The Eliashberg function directly affects the effective mass of the charge carriers in the metallic state, reveals the frequencies and coupling strength of the relevant phonons[16], and enters into the Migdal-Eliashberg theory of superconductivity[17]. In general, the Eliashberg function is an anisotropic function of the electron momentum[18]; for example, $MgB_2$ is an anisotropic superconductor with one of the highest ambient-pressure phonon-mediated critical temperatures of $T_c$ = 39 K[19]. Its two superconducting gaps originate from the out-of-plane $\sigma$-state Fermi sheets and the two in-plane tubular structures arising from the $\pi$ states[7,20].

The Eliashberg function is accessible through experimental techniques, including optical-conductivity experiments[21], electron tunneling[22], Landau level spectroscopy[23], and angle-resolved photoemission spectroscopy (ARPES)[24]. However, optical-conductivity experiments and electron tunneling only provide access to the isotropic Eliashberg function, making

[1]European Theoretical Spectroscopy Facility, Institute of Condensed Matter and Nanosciences, Université catholique de Louvain, Louvain-la-Neuve, Belgium. [2]Department of Quantum Matter Physics, University of Geneva, Geneva, Switzerland. [3]U Bremen Excellence Chair, Bremen Center for Computational Materials Science, and MAPEX Center for Materials and Processes, University of Bremen, Bremen, Germany. [4]Theory and Simulation of Materials (THEOS), and National Centre for Computational Design and Discovery of Novel Materials (MARVEL), École Polytechnique Fédérale de Lausanne, Lausanne, Switzerland. [5]Laboratory for Materials Simulations, Paul Scherrer Institut (PSI), Villigen, Switzerland. [6]Institut de Physique, École Polytechnique Fédérale de Lausanne, Lausanne, Switzerland. [7]Center for Photon Science, Paul Scherrer Institut (PSI), Villigen, Switzerland. [8]WEL Research Institute, Wavre, Belgium. ✉e-mail: thomas@vanwaas.org; samuel.ponce@uclouvain.be

ARPES the experimental method of choice for accessing anisotropic EPC. In an ARPES experiment, photoelectrons are ejected out of a material via the photoelectric effect[25], after which their kinetic energies and emission angles are detected[26]. The kinetic energy is then related to the electronic binding energy and the angle to the momentum, via conservation equations[26]. Recent progress has made the spin degree of freedom also accessible via high-accuracy spin-ARPES[27,28]. The effect of anisotropic EPC on an electron in the $n^{\text{th}}$ band at wavevector $\mathbf{k}$ is described by a complex quantity known as the electron self-energy $\Sigma_n(E,\mathbf{k}) = \Sigma'_n(E,\mathbf{k}) + \mathrm{i}\Sigma''_n(E,\mathbf{k})$[3] where $\Sigma_n$ is an abbreviation for the band-diagonal $\Sigma_{nn}$[29]. The real part $\Sigma'_n(E,\mathbf{k})$ renormalizes the eigenenergy of an electron from the non-interacting dispersion $\varepsilon_n(\mathbf{k})$ into $E_n(\mathbf{k}) = \varepsilon_n(\mathbf{k}) + \Sigma'_n(E_n(\mathbf{k}),\mathbf{k})$, whereas the imaginary part $\Sigma''_n(E,\mathbf{k})$ defines a lifetime $\tau_n(\mathbf{k})$ via $\hbar/\tau_n(\mathbf{k}) = -2\Sigma''_n(E_n(\mathbf{k}),\mathbf{k})$[16], where $\hbar$ is the reduced Planck constant, which after energy renormalization gives the quasiparticle lifetime. The self-energy and non-interacting dispersion enter into the electronic spectral function $A_n(E,\mathbf{k})$[30], which can be interpreted as a momentum- and band-resolved density of states (DOS).

To gain fundamental insight into the intrinsic EPC of materials, it is desirable to extract the electron self-energy from an ARPES band map. This extraction is often performed by fitting momentum-distribution curves (MDCs), during which the momentum dependence of the self-energy is neglected[31], giving rise to an extracted self-energy $\Sigma_n(E)$ for a specific momentum cut and branch index, collectively labeled as $n$. Here, we call "branch" a dispersing feature of a band map that can be singled out during the MDC fitting, where it is jointly described by $\varepsilon_n(\mathbf{k})$ and $\Sigma_n(E)$. In this process, $\varepsilon_n(\mathbf{k})$ of such a branch is usually approximated by a polynomial dispersion and sometimes obtained from first-principles calculations[32]. The spectral function $A_n(E,\mathbf{k})$ is often approximated by a Lorentzian as a function of $\mathbf{k}$, which is exact only when $\Sigma_n(E,\mathbf{k})$ is momentum-independent, and $\varepsilon_n(\mathbf{k})$ is linear in $\mathbf{k}$[31]. The angular/momentum resolution during the MDC fitting is usually incorporated by convolving each Lorentzian peak with a Gaussian, leading to a Voigt profile[33]. Given that many non-interacting dispersions are non-linear, the use of Lorentzians leads to a biased extraction of $\Sigma_n(E)$[34]. In this work, we propose a more general approach based on non-interacting dispersions described by polynomials, which improves the self-energy extraction when the dispersion relation is notably non-linear, as is the case for, e.g., $Sr_2RuO_4$[35] or $SrMoO_3$[36].

A common treatment of EPC expands $\Sigma_n^{\text{ph}}(E,\mathbf{k})$ to lowest order in the reciprocal of the atomic mass, which includes the dynamical Fan-Migdal term $\Sigma_n^{\text{FM}}(E,\mathbf{k})$[37,38], as well as the static Debye-Waller term $\Sigma_n^{\text{DW}}(\mathbf{k})$[39,40] and the tadpole/polaron term $\Sigma_n^{\text{P}}(\mathbf{k})$[41,42]. We argue here that for photoemission kinks, $\Sigma_n(E)$ is often dominated by the Fan-Migdal contribution $\Sigma_n^{\text{FM}}(E)$, from which one can extract the Eliashberg function $\alpha^2F_n(\omega)$ with phonon energy $\omega$, which combines the phonon DOS $F(\omega)$ with a coupling function $\alpha_n^2(\omega)$[43]. Furthermore, we argue that purely static, real-valued self-energies such as $\Sigma_n^{\text{DW}}(\mathbf{k})$ should be captured by $\varepsilon_n(\mathbf{k})$ during the fit. ARPES can therefore give access to anisotropic EPC through analysis of $\Sigma_n^{\text{FM}}(E)$ along different momentum paths.

Some of the first determinations of $-\Sigma''_n(E)$ from ARPES band maps were performed for elemental metals in the mid-1990s[44,45], while one of the first extractions of $\Sigma'_n(E)$ was performed for $Bi_2Sr_2CaCu_2O_{8+\delta}$ in 1999[46]. Furthermore, in 2004, Shi et al.[15] were among the first to obtain $\alpha^2F_n(\omega)$ by solving an inversion problem for $\Sigma'_n(E)$ for a branch of the $(10\bar{1}0)$ Be shallow $\bar{\text{A}}$-point surface state using the maximum-entropy method (MEM)[47], establishing ARPES as the method of choice to quantify anisotropic EPC. The MEM allows for the incorporation of prior knowledge in $\alpha^2F_n(\omega)$, such as positive semidefiniteness over a finite bandwidth[15]. In subsequent years, $\alpha^2F_n(\omega)$ was extracted for a wide range of materials, including a Be(0001) surface state[48], $MgB_2$[49], doped graphene[50–56], the kagome metal $CsV_3Sb_5$[57], the two-dimensional electron liquid (2DEL) of Nb-doped $SrTiO_3$[58], a Ni(111) surface state also including electron-magnon coupling[59], and several cuprates[60–62]. In parallel to the experimental investigations into EPC, first-principles methods have grown into a powerful tool to simulate electronic band structures using density-functional theory (DFT) and beyond[63], as well as phonon energies and EPC from density-functional perturbation theory (DFPT)[29,64–66]. Calculations of the latter have become computationally feasible by momentum extrapolation[67], Fourier interpolation of the perturbed potential[68,69], or Wannier interpolation[70,71] of the EPC matrix elements[72], nowadays implemented in various first-principles codes[7,69,73–78]. State-of-the-art developments in the calculation of $\Sigma_n^{\text{ph}}(E)$ include a description of the perturbation of the electronic potential at the GW level[79] and a description of the electron's Green's function at the level of dynamical mean-field theory (DMFT)[80]. Thus, the time is ripe for the treatment of ARPES data in a many-body framework and to connect $\Sigma_n^{\text{FM}}(E)$ and $\alpha^2F_n(\omega)$ from ARPES to their first-principles counterparts.

Matthiessen's rule states that $\Sigma_n(E) = \Sigma_n^{\text{ph}}(E) + \Sigma_n^{\text{el}}(E) + \Sigma_n^{\text{imp}}(E)$[81,82], with $\Sigma_n^{\text{el}}(E)$ and $\Sigma_n^{\text{imp}}(E)$ the respective electron-electron and electron-impurity contributions. A key problem in determining $\Sigma_n^{\text{ph}}(E)$ from $A_n(E,\mathbf{k})$ is that $\varepsilon_n(\mathbf{k})$, $\Sigma_n^{\text{el}}(E)$, and $\Sigma_n^{\text{imp}}(E)$ are unknown. To distinguish between $\varepsilon_n(\mathbf{k})$ and $\Sigma_n(E)$, the current state of the art relies on the Kramers-Kronig relations between $\Sigma'_n(E)$ and $\Sigma''_n(E)$[6]. Typically, one makes an initial guess of a linear $\varepsilon_n(\mathbf{k})$ leading to $\Sigma'_n(E)$ and $-\Sigma''_n(E)$; the Kramers-Kronig relations are then used to obtain $\Sigma'_n(E)$ as the Hilbert transform of $\Sigma''_n(E)$, which is then compared to the initial $\Sigma'_n(E)$. The non-interacting parameters are then obtained by minimizing the difference between the two $\Sigma'_n(E)$[31,54,83,84], a procedure sometimes referred to as the Kramers-Kronig bare-band fitting (KKBF)[31]. However, in practice, an ARPES band map yields a finite, noisy set $\{\Sigma_n(E)\}$, such that the transform of $\Sigma'_n(E)$ will not perfectly reconstruct $\Sigma''_n(E)$, and some expression for $-\Sigma''_n(E)$ must be assumed outside the fitted range to perform the Hilbert integral. Several Python codes are readily available for the treatment of ARPES data, such as PyARPES[85], pesto[86], NavARP[87], and ERLabPy[88]. While these codes offer advanced data visualization capabilities, their many-body functionality is generally limited to extracting $\Sigma_n(E)$ for a single linear dispersion relation without matrix-element correction, and no decomposition into $\Sigma_n^{\text{ph}}(E)$, $\Sigma_n^{\text{el}}(E)$, or $\Sigma_n^{\text{imp}}(E)$ is available.

In this work, we describe a consistent way to extract $\Sigma_n(E)$ for parabolic non-interacting dispersions, which can be extended to bands described by polynomials of all orders. Next, we show how to extract $\alpha^2F_n(\omega)$ from $\Sigma_n(E)$ and demonstrate with an artificial example that this inversion monotonically converges towards the true result for a sufficient amount of unbiased data. Specifically, we extend the MEM with Bayes' rule[89] to determine the non-interacting dispersion parameters and the magnitudes of $\Sigma_n^{\text{el}}(E)$ and $\Sigma_n^{\text{imp}}(E)$ from the most probable $\alpha^2F_n(\omega)$[89], eliminating human bias from their evaluation. We aim to describe these quantities in a terminology that unifies experimental and first-principles communities, and we show how the experimental quantities for $\varepsilon_n(\mathbf{k})$, $\Sigma_n(E)$, $\alpha^2F_n(\omega)$ are related to their first-principles counterparts. We distribute these novel functionalities in the first release of the GPLv3-licensed code xARPES v1.0.0.

In the Results section, we introduce the photointensity containing $A_n(E,\mathbf{k})$, show how to obtain $\Sigma_n(E)$ in the presence of a parabolic $\varepsilon_n(\mathbf{k})$, and provide expressions for $\Sigma_n(E)$ from impurity, electron, and phonon interactions. We then show how a one-shot solution for $\alpha^2F_n(\omega)$ can be obtained from $\Sigma_n(E)$, or alternatively how $\Sigma_n(E)$, $\alpha^2F_n(\omega)$, and the model parameters can be iteratively obtained with Bayesian inference. We then illustrate the different capabilities of the code with three examples: a model system, and two case studies of $TiO_2$-terminated $SrTiO_3$ and of Li-doped graphene, which are also distributed as xARPES example Jupyter notebooks. In the Discussion section, we summarize our findings and provide an overview of future directions on the subject, including the use of approximated non-interacting dispersions from DFT, which may aid the first-principles community by offering controlled reference data to benchmark new and existing approaches.

## Results

### Angle-resolved photoemission spectroscopy

First, we introduce the experimental geometry of a typical ARPES experiment—as displayed in Fig. 1—with electrons collected along a detector slit characterized by an angle $\eta$. Photons of energy $h\nu$, with $h$ the Planck constant and $\nu$ the photon frequency, illuminate the material at an incident light

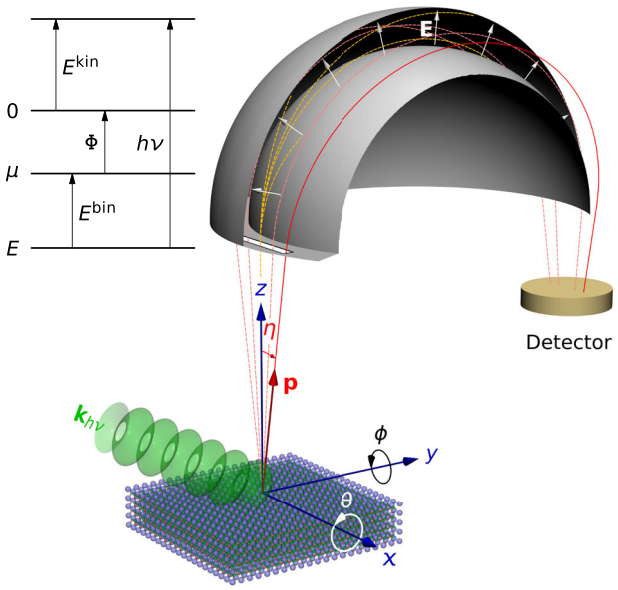


**Fig. 1 | ARPES geometry and energy diagram.** Light reaches the material, leading to emission of photoelectrons, where a selection passes through a hemispherical analyzer and gets detected. The inset shows an energy diagram for the one-step photoemission process. The displayed variables are defined in the main text.

wavevector $\mathbf{k}_{h\nu}$. The material contains electrons with a distribution of energies $E$, yielding a binding energy $E^{\text{bin}} = \mu - E$ with respect to the chemical potential $\mu$, where we set the vacuum energy at the analyzer to zero. When $h\nu$ is sufficiently high for electrons to reach the vacuum energy at the sample, photoelectrons of rest mass $m_e$ are detected with kinetic energies $E^{\text{kin}} = h\nu - \Phi - E^{\text{bin}}$, with $\Phi$ the work function. In a typical ARPES setup, the chemical potentials of the sample and the analyzer are aligned, while the vacuum level at the detector serves as the zero of energy, such that $\Phi$ can be identified as the work function of the analyzer[90]. Far from the sample, the wavefunctions of the photoemitted electrons can be approximated by plane waves with momenta $\hbar\mathbf{p}$ and energies $E^{\text{kin}} = \hbar^2|\mathbf{p}|^2/(2m_e)$. A radial electric field $\mathbf{E}$ is applied within the hemispherical analyzer, such that electrons arrive at the detector with $E^{\text{kin}}$ within the energy resolution.

During the experiment, electrons enter a hemispherical analyzer through a detector slit characterized by an angle $\eta$. Figure 1 shows the situation where the normal vector of the material and the normal vector of the detector lie along the same axis, with electrons collected at the detector angle $\eta$ in the $xz$-plane. Rotations of the sample along the $x$- and $y$-axes are described by the angles $\theta$ and $\phi$, respectively. Potentially, the set of accessible material rotations can be completed by including a rotation about the $z$ axis[91]. Following these conventions, the components of $\mathbf{p}$ are given by:

$$\mathbf{p} = |\mathbf{p}| \begin{pmatrix} \cos(\phi)\sin(\eta) + \sin(\phi)\cos(\theta)\cos(\eta) \\ \sin(\theta)\cos(\eta) \\ \sin(\phi)\sin(\eta) + \cos(\phi)\cos(\theta)\cos(\eta) \end{pmatrix}, \tag{1}$$

where $|\mathbf{p}| = \sqrt{2m_e E^{\text{kin}}/\hbar^2}$. When $\theta = 0$, $p_x = |\mathbf{p}|\sin(\eta + \phi)$, such that $p_x$ can directly be calculated after correcting with $\phi$, either to correct for misalignment or to cover a larger portion of reciprocal space. The in-plane momentum is conserved in the photoemission process, so that the in-plane components $k_x$ and $k_y$ can be inferred from $\eta$, $\theta$, and $\phi$.

The ARPES experiment can be described using photoemission theories at different levels of approximation. Early models based on a phenomenological three-step decomposition[92] were superseded in the 1970s by a fundamental one-step theory that describes photoemission as a single quantum-mechanical process[93–96]. Although formally rigorous, the fundamental theory is intractable when applied to real materials. Therefore, it is usually replaced by a simpler one-step description, where the steady-state photoelectron flux is regarded as a transition rate computed using Fermi's golden rule[24,97,98]. Each possible final state of the transition is written as a product of a sample eigenstate and the photoelectron wavefunction. This factorization enables separating the spectroscopic properties of the sample —represented by the spectral function—from geometric factors related to the photoelectron wavefunction that are gathered in a matrix element. For a crystalline surface, the transition rate has the form[24]:

$$w(E,\mathbf{p}) = \frac{2\pi}{\hbar}\sum_{n\mathbf{k}} |M_n(\mathbf{p},\mathbf{k})|^2 \delta_{\mathbf{k}_\parallel,\check{\mathbf{p}}_\parallel} A_n(E,\mathbf{k}) f(E), \tag{2}$$

where the sum runs over all Bloch waves with band index $n$ and wavevector $\mathbf{k}$ within the first Brillouin zone. In Eq. (2), $M_n(\mathbf{p},\mathbf{k})$ is the matrix element of the light-matter coupling between the Bloch wave and the photoelectron state identified by its wavevector $\mathbf{p}$. The notation of Eq. (2) emphasizes the conservation of in-plane crystal momentum at an ideal planar surface, where the in-plane wavevector $\mathbf{k}_\parallel$ of the Bloch state matches the vector corresponding to $\mathbf{p}_\parallel$ within the first Brillouin zone, here denoted $\check{\mathbf{p}}_\parallel$. As a consequence, changing $\mathbf{p}$ by an in-plane reciprocal lattice vector $\mathbf{G}_\parallel$, corresponding to a higher Brillouin zone, will affect the matrix element but not the spectral function, which has the periodicity of the lattice. The dependence of $M_n(\mathbf{p},\mathbf{k})$ on $\mathbf{k}_\perp$ and $\mathbf{p}_\perp$ is set by the material-specific wave functions and depends on $h\nu$ and the light polarization $\boldsymbol{\epsilon}$. The photoemission matrix element (PME) is often assumed to be peaked at $\mathbf{k}_\perp = \check{\mathbf{p}}_\perp$[99,100], with a span of the order of $\ell_e^{-1}$, where $\ell_e$ is the photoelectron escape depth. $A_n(E,\mathbf{k})$ is the spectral function evaluated at the initial energy $E$ of the photoelectron (see inset of Fig. 1), which includes the non-interacting dispersion and the self-energy discussed in the Introduction section:

$$A_n(E,\mathbf{k}) = \frac{1}{\pi}\frac{-\Sigma_n''(E,\mathbf{k})}{[E - \varepsilon_n(\mathbf{k}) - \Sigma_n'(E,\mathbf{k})]^2 + [\Sigma_n''(E,\mathbf{k})]^2}. \tag{3}$$

Non-interacting electrons have all the spectral weight at the band energy, corresponding to $\Sigma_n(E,\mathbf{k}) = -i0^+$ and $A_n(E,\mathbf{k}) = \delta(E - \varepsilon_n(\mathbf{k}))$. Sufficiently weak interactions preserve this peak structure, but broaden the $\delta$-function while shifting it to the quasiparticle energy $E_n(\mathbf{k})$. The broadening corresponds to the lifetime via $\hbar/\tau_n(\mathbf{k}) = -2\Sigma_n''(E_n(\mathbf{k}),\mathbf{k})$ and may be expressed in terms of a mean free path $\boldsymbol{\ell}_n(\mathbf{k}) \equiv \mathbf{v}_n(\mathbf{k})\tau_n(\mathbf{k})$ via the group velocity $\mathbf{v}_n(\mathbf{k}) = \hbar^{-1}\nabla E_n(\mathbf{k})$. The last factor in Eq. (2) is the Fermi-Dirac distribution $f(E) \equiv [e^{(E-\mu)/(k_B T)} + 1]^{-1}$ with $k_B$ the Boltzmann constant and $T$ the temperature, representing the requirement that the photoelectron state is initially occupied.

The spectral function of surface states and of states in two-dimensional (2D) systems is independent of $\mathbf{k}_\perp$. As a result, $w$ factorizes into a part involving the matrix element and a part involving the spectral function. Such a factorization is, in general, impossible for three-dimensional (3D) states, such as the $\sigma$-state sheets of $MgB_2$[20], since the sum over $\mathbf{k}_\perp$ in Eq. (2) mixes the matrix element with the spectral function. The factorization is nevertheless possible if either $\ell_e \gg |\boldsymbol{\ell}_n|$ or $|\boldsymbol{\ell}_n| \gg \ell_e$. In the first regime, the matrix element is sharply peaked at $\mathbf{k}_\perp = \check{\mathbf{p}}_\perp$, while in comparison, the spectral function varies slowly around $\mathbf{k}_\perp$ with a span of order $|\boldsymbol{\ell}_n^{-1}|$. Thus, the matrix element enforces approximate conservation of perpendicular momentum, and the spectral function is evaluated at $\mathbf{k}_\perp = \check{\mathbf{p}}_\perp$. If $|\boldsymbol{\ell}_n| \gg \ell_e$, the spectral function is sharp and the matrix element is broad, such that $w$ is proportional to the surface-projected spectral function $\sum_{\mathbf{k}_\perp} A_n(E,\mathbf{k})$, leading to intrinsic broadening of the spectral features. In many 3D systems, neither of these two regimes is realized, and the matrix element and spectral function are inextricably mixed. As this work focuses on the self-energy of 2D systems and surface states, we adopt the product ansatz and we treat the matrix element as a phenomenological ingredient.

The experimental band map is recorded through a detector slit characterized by an angle $\eta$ while selecting and counting photoelectrons according to their kinetic energy. As $E^{\text{kin}} = h\nu - \Phi + E - \mu$, the photoelectron wavevector may be viewed as a function $\mathbf{p}(E,\eta)$ of the two variables

$E$ and $\eta$. Due to finite energy and angular resolutions of the hemispherical analyzers[101], the measured intensity is convolved with resolution functions $R(E)$ and $Q(\eta)$ with full widths at half maximum (FWHM) $\Delta E$ and $\Delta\eta$, which are usually taken to be Gaussian distributions. Taking into account an energy- and possibly weakly angle-dependent background $B(E,\eta)$, we arrive at the photointensity at light polarization $\boldsymbol{\epsilon}$ as the time-integrated transition rate:

$$P(E,\eta;h\nu,\boldsymbol{\epsilon}) \propto \int_{-\infty}^{\infty} \mathrm{d}E'\, R(E-E') \int_{-\infty}^{\infty} \mathrm{d}\eta'\, Q(\eta-\eta') \times \left[ B(E',\eta') + f(E') \sum_n |M_n(E',\eta';h\nu,\boldsymbol{\epsilon})|^2 A_n(E',\eta') \right]. \quad (4)$$

The photointensity at fixed $\eta$ yields an energy-distribution curve (EDC), and the photointensity at fixed $E$ yields an MDC. After specifying the rotation angles displayed in Fig. 1, the $\eta$-dependent quantities in Eq. (4) can be converted into $\mathbf{k}$-dependent quantities.

### xARPES workflow

In this section, we give an overview of the different steps that can be performed with the xARPES code. The workflow is displayed in Fig. 2, where boxes describe individual steps of the code and refer to the sections in which these steps are described in detail. The first step is to load raw photointensity data for a given photon energy $h\nu$ and polarization $\boldsymbol{\epsilon}$.

After loading the band map containing data in $E^{\mathrm{kin}}$, the user can either perform a Fermi-edge fit or provide a previous Fermi-edge fit result, which gives the electron energy $E$ in the photointensity $P(E,\eta)$. Next, the user selects a region from the band map to be used for MDC fitting—with discrete energies indexed as $E_j$—and selects a set of linear/curved dispersions indexed with $n$ to be fitted in this region. When using parabolic non-interacting dispersions, the locations of the band extrema must also be provided, either as an angle $\eta_n^{\mathrm{c}}$ or wavevector $k_n^{\mathrm{c}}$. Next, the code fits the MDCs to capture the band map information in terms of the dimensionless peak positions $\widetilde{r}_n(E_j)$ and peak widths $\widetilde{\gamma}_n(E_j)$, where the tilde (~) refers to fitted quantities. Afterwards, initial guesses (denoted with 0) for the real $(\widetilde{\Sigma}'_{n0}(E_j))$ and minus imaginary parts $(-\widetilde{\Sigma}''_{n0}(E_j))$ of the self-energy are calculated by merging these fitting results with initial guesses for the non-interacting band parameters, such as the Fermi wavevector $k_{n0}^{\mathrm{F}}$. If a photoemission kink is present in the phonon contribution to $\widetilde{\Sigma}'_{n0}(E)$, the user may wish to extract the Eliashberg function $\alpha^2F_{n0}(\omega)$ with the Maximum-Entropy Method (MEM) implemented in xARPES. In the one-shot mode, extraction of $\alpha^2F_{n0}(\omega)$ requires the user to assign the magnitude of the electron-electron coupling coefficient $\lambda_{n0}^{\mathrm{el}}$ and minus the imaginary part of the impurity contribution to the electron self-energy $\Gamma_{n0}^{\mathrm{imp}}$. After obtaining the one-shot results with the initial guesses for the model parameters—including the non-interacting band parameters and the electron and impurity contributions—the Bayesian inference loop can be called for a full optimization of the parameters. This full optimization also results in the final $\alpha^2F_n(\omega)$, from which $\Sigma_n(E)$ can be calculated at every $E$. Optionally, the results can be improved by repeating the above code steps for various $k_n^{\mathrm{c}}$, followed by choosing the most probable result from the individual optimizations. Finally, we remark that while $\alpha^2F_{n0}(\omega)$ is traditionally extracted using only $\widetilde{\Sigma}'_{n0}(E_j)$, xARPES provides the possibility of employing $\widetilde{\Sigma}'_{n0}(E_j)$, $-\widetilde{\Sigma}''_{n0}(E_j)$, or both.

### Extraction of the self-energy

We consider photoemission kinks of electronic bands that are sufficiently far from other bands to ignore band mixing[102], such that they can be described as individual branches $n$, starting out with Eqs. (3) and (4). The MDC fitting is performed in $\eta$-space instead of wavevector space, because the angular resolution of the detector $\Delta\eta$ is approximately constant as a function of $\eta$. A wavevector-based fitting will be implemented in a future version of xARPES, which will be useful when the desired momentum-space path is poorly parameterized by a single angle, such as for cuts through 3D data sets. The photoelectron wavevector $\mathbf{p}(E,\eta)$ is mapped to the crystal wavevector $\mathbf{k}(E,\eta)$ in the first Brillouin zone. This is accurate for 2D states, which have no dispersion along $\mathbf{k}_\perp$, but ignores a broadening in $\mathbf{k}_\perp$ for 3D states. The MDCs are created as different slices of the band map, after which the branches labeled with $n$ are fitted on the selected angular range, leading to extraction of $\Sigma_n(E_j)$ from MDC fits at selected energies $E_j$, with $j$ the MDC index. The momentum dependence of the self-energy is ignored during the MDC fitting, resulting in a fitted self-energy $\Sigma_n(E)$. Therefore, the non-interacting band $\varepsilon_n(\mathbf{k})$ is the only momentum-dependent quantity during the fitting. As a consequence, any purely static, real-valued self-energy contributions $\Sigma'_n(\mathbf{k})$ from the true self-energy are likely captured by $\varepsilon_n(\mathbf{k})$ instead of $\Sigma'_n(E)$. If the MDC presents a sufficiently sharp single peak at wavevector $\mathbf{k}_n(E_j)$, the fitting is mostly sensitive to the self-energy in the vicinity of $\mathbf{k}_n(E_j)$. The solutions $\Sigma_n(E_j)$ should then be regarded as an experimental determination of the self-energies $\Sigma_n(E_j,\mathbf{k}_n(E_j))$[103,104]. Thus, when comparing to theoretical calculations (calc), the experimental $\varepsilon_n(\mathbf{k})$ should be compared to the sum of the non-interacting dispersion and static

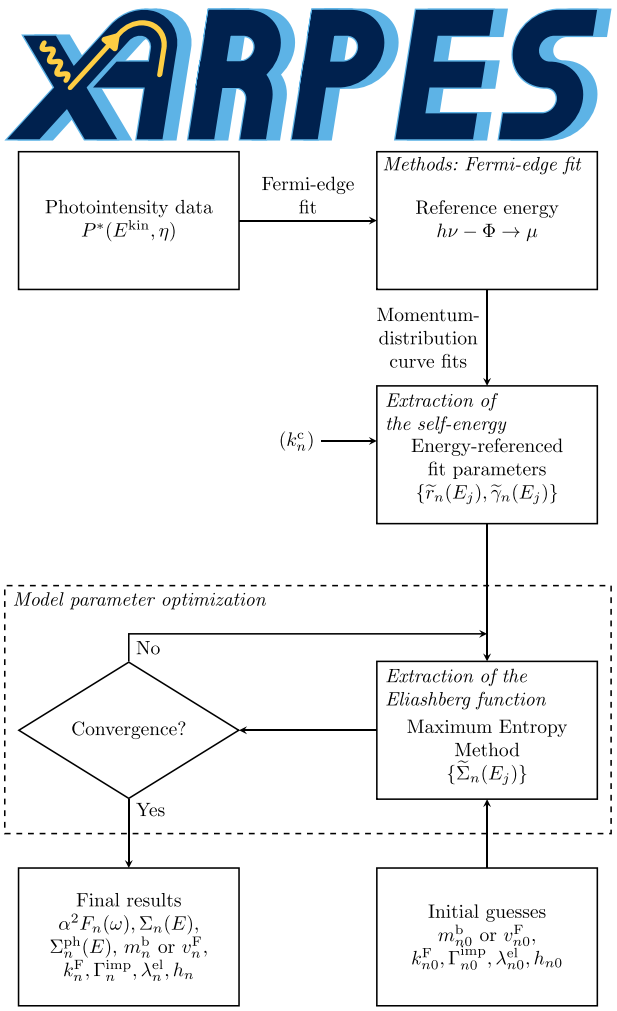


**Fig. 2 | xARPES logo and flowchart.** Different steps of the workflow are described in detail in the text. The workflow can be divided into three parts. First, the Fermi edge and the momentum-distribution curves from photointensity data $P^*(E^{\mathrm{kin}},\eta)$ are fitted to obtain the respective peak positions and widths $\{\widetilde{r}_n(E_j),\widetilde{\gamma}_n(E_j)\}$. Second, initial guesses for the model parameters are inserted into the maximum-entropy method to obtain the one-shot self-energy $\Sigma_{n0}(E)$ and Eliashberg function $\alpha^2F_{n0}(\omega)$. Third, the optimization loop can be called to obtain the optimized self-energy $\Sigma_n(E)$ and Eliashberg function $\alpha^2F_n(\omega)$. The boxes contain the variables and are tagged with the subsection in which the step is fully described. The subsections belong to the Results section unless described as a "Methods" section.

self-energy $\varepsilon_n^{\mathrm{calc}}(\mathbf{k}) + \Sigma_n^{\mathrm{calc}'}(\mathbf{k})$, while $\Sigma_n(E)$ should be compared to the dynamical $\Sigma_n^{\mathrm{calc}}(E, \mathbf{k})$ evaluated at the momentum $\mathbf{k}$ corresponding to the quasiparticle energy $E_n^{\mathrm{calc}}(\mathbf{k})$ closest to $E$.

We start from the photointensity in Eq. (4) with fixed $\boldsymbol{\epsilon}$ and $h\nu$, where $n$ is now a branch index, and assume that the PME depends more strongly on $\eta$ than on $E$, which results in $|M_n(E, \eta; h\nu, \boldsymbol{\epsilon})|^2 \to |M_n(\eta)|^2$, which is a dimensionless quantity that the user can set manually. We refer to the use of a non-constant $|M_n(\eta)|^2$ during the MDC fitting as the matrix-element correction (MEC). For the MDC $j$, we approximate the $E_j^{\mathrm{kin}}$-referenced photointensity $P^*(E_j^{\mathrm{kin}}, \eta)$ from Eq. (4) with an expression $\widetilde{P}(E_j^{\mathrm{kin}}, \eta)$ for which the energy convolution is neglected:

$$\widetilde{P}(E_j^{\mathrm{kin}}, \eta) = \int_{-\infty}^{\infty} \mathrm{d}\eta' Q(\eta - \eta') \left\{ \widetilde{B}(E_j^{\mathrm{kin}}, \eta') + \sum_n |M_n(\eta')|^2 \times \frac{\widetilde{\mathcal{A}}_n^0(E_j)}{\pi} \frac{-\widetilde{\Sigma}_n''(E_j) E_{\mathrm{dim}}}{\left[E_j - \varepsilon_n(\eta') - \widetilde{\Sigma}_n'(E_j)\right]^2 + \left[\widetilde{\Sigma}_n''(E_j)\right]^2} \right\}, \tag{5}$$

where $E_{\mathrm{dim}}$ is constant with dimensions of an energy and $\widetilde{B}(E_j^{\mathrm{kin}}, \eta)$ is a user-defined polynomial in $\eta$, which is fitted for each $E_j^{\mathrm{kin}}$. In Eq. (5), $\widetilde{\mathcal{A}}_n^0(E_j)$ and $\widetilde{B}(E_j^{\mathrm{kin}}, \eta)$ have units of photointensity, while the relation $E_j^{\mathrm{kin}} = h\nu - \Phi + E_j - \mu$ can be established after $h\nu - \Phi$ has been determined from the Fermi-edge fit. Interestingly, a convenient rewriting allows for eliminating two of the $l + 1$ fitting parameters of a non-interacting band described by a polynomial of order $l$ during the fitting procedure. Consequently, a parabolic dispersion can be fitted with one parameter, which in xARPES is either the wavevector of the extremum $k_n^{\mathrm{c}}$ or the corresponding angle $\eta_n^{\mathrm{c}}(E)$ at $E = \mu$, with no parameters needed for a linear non-interacting dispersion. As an example, we perform the convenient rewriting for a parabolic dispersion, with example analyses provided in the Verification using model data and Photoemission matrix elements in $TiO_2$-terminated $SrTiO_3$ sections. The implementation works for electron-like (positive mass) as well as hole-like (negative mass) bands. The code also supports the linear case, which is presented in Supplementary Section S1.

Here—and in the first release of xARPES—we assume that the parallel momentum $p_\parallel$ of the photoelectron is related to the detector angle $\eta$ as:

$$p_\parallel = \sqrt{2 m_{\mathrm{e}} E^{\mathrm{kin}}/\hbar^2}\, \sin(\eta + \phi). \tag{6}$$

The parallel component in Eq. (6) can be obtained from the $x$-component in Eq. (1) by using a possible rotation around the $z$-axis, and by subtraction of the angle $\phi$, after which we denote $\eta + \phi \to \eta$ for brevity. Thus, Eq. (6) describes detection along all planes that contain the normal vector of the material, with more complicated expressions for $p_\parallel$ scheduled for future releases of xARPES. A generic parabolic dispersion along this path may be written as:

$$\varepsilon_n(\eta) = \mu + \frac{m_{\mathrm{e}}}{m_n^{\mathrm{b}}} E^{\mathrm{kin}} \left\{ [\sin(\eta) - \sin(\eta_n^{\mathrm{c}})]^2 - \sin^2(\eta_n^{\mathrm{F}}) \right\}, \tag{7}$$

where $m_n^{\mathrm{b}}$ is the mass of the non-interacting band, and the angles $\eta_n^{\mathrm{c}}$ and $\eta_n^{\mathrm{F}}$ are related to the projected centers $k_n^{\mathrm{c}}$ and Fermi wavevectors $k_n^{\mathrm{F}}$ of the parabola by $\sin^2(\eta_n^{\mathrm{c}}) = (\hbar k_n^{\mathrm{c}})^2/(2 m_{\mathrm{e}} E^{\mathrm{kin}})$ and $\sin^2(\eta_n^{\mathrm{F}}) = (\hbar k_n^{\mathrm{F}})^2/(2 m_{\mathrm{e}} E^{\mathrm{kin}})$, respectively. The branch label $n$ takes into account the momentum path of Eq. (6) such that the band parameters $k_n^{\mathrm{F}}$, $m_n^{\mathrm{b}}$, and $k_n^{\mathrm{c}}$ are projected onto the momentum path, and the same underlying band may result in different projected parameters along a different path. With $\varepsilon_n(\eta)$ given by Eq. (7), Eq. (5) becomes:

$$\widetilde{P}(E_j^{\mathrm{kin}}, \eta) = \int_{-\infty}^{\infty} \mathrm{d}\eta' Q(\eta - \eta') \left\{ \widetilde{B}(E_j^{\mathrm{kin}}, \eta') + \sum_n |M_n(\eta')|^2 \times \frac{\widetilde{\mathcal{A}}_n^0(E_j)}{\pi} \frac{\widetilde{\gamma}_n(E_j)}{\left\{ \left[\sin(\eta') - \sin(\eta_n^{\mathrm{c}}(E_j))\right]^2 - \widetilde{r}_n^2(E_j) \right\}^2 + \widetilde{\gamma}_n^2(E_j)} \right\}, \tag{8}$$

after which the self-energy data can be computed via:

$$\widetilde{\Sigma}_n'(E_j) = E_j - \mu - \frac{m_{\mathrm{e}}}{m_n^{\mathrm{b}}} E_j^{\mathrm{kin}} [\widetilde{r}_n^2(E_j) - \sin^2(\eta_n^{\mathrm{F}})], \tag{9}$$

$$-\widetilde{\Sigma}_n''(E_j) = \frac{m_{\mathrm{e}}}{|m_n^{\mathrm{b}}|} E_j^{\mathrm{kin}} \widetilde{\gamma}_n(E_j), \tag{10}$$

where $\widetilde{\gamma}_n(E_j)$ is a dimensionless broadening parameter, and $\widetilde{r}_n(E_j)$ is a dimensionless peak maximum relative to $\sin(\eta_n^{\mathrm{c}}(E_j))$. Furthermore, the prefactors in Eqs. (5) and (8) are related by $\widetilde{\mathcal{A}}_n^0(E_j) = \widetilde{A}_n^0(E_j) m_{\mathrm{e}} E_j^{\mathrm{kin}}/(|m_n^{\mathrm{b}}| E_{\mathrm{dim}})$. The MDC maxima can then be recovered by assigning the fitted quantities to the left-hand or right-hand side of a parabola. Eq. (8) allows for fitting the MDCs with the dimensionless quantities $\widetilde{\gamma}_n(E_j)$ and $\widetilde{r}_n(E_j)$, while the fit no longer has to be performed with $m_n^{\mathrm{b}}$ and $k_n^{\mathrm{F}}$. The rewriting also simplifies finding a sufficiently good initial guess for the MDC fitting, as the angular distance between $\widetilde{r}_n(E_j)$ and $\sin(\eta_n^{\mathrm{c}}(E_j))$ can directly be visualized.

Once the fitting parameters $\{\widetilde{r}_n(E_j), \widetilde{\gamma}_n(E_j)\}$ have been obtained, they can be substituted into Eqs. (9) and (10) to obtain the extracted self-energy $\widetilde{\Sigma}_n(E_j)$. In this process, $m_n^{\mathrm{b}}$ and $k_n^{\mathrm{F}}$ may either be provided by the user in the one-shot mode, or they can be optimized through the Bayesian inference feature of xARPES described in the Model parameter optimization subsection.

### Extraction of the Eliashberg function

In this section, we describe how the Eliashberg function $\alpha^2 F_n(\omega)$ can be extracted from $\widetilde{\Sigma}_n(E)$ for a given set of parameters, whose optimization is described in the Model parameter optimization subsection. Considering phonons as the only type of coupling bosons, we assume validity of Matthiessen's rule[81,82], which implies that $\Sigma_n(E)$ can be decomposed into the following contributions:

$$\Sigma_n(E) = \Sigma_n^{\mathrm{ph}}(E) + \Sigma_n^{\mathrm{el}}(E) + \Sigma_n^{\mathrm{imp}}(E). \tag{11}$$

Matthiessen's rule implies that mixed contributions, as for example an electron propagator renormalized by electron-electron interactions in the lowest-order electron-phonon coupling diagram[80], are negligible. The rule applies if all couplings are in the perturbative regime and if the self-energy is evaluated at leading order in each of them, since the mixed terms are of higher orders.

In xARPES, the impurity contribution to the electron self-energy $\Sigma_n^{\mathrm{imp}}(E)$ is fitted with an imaginary static decay rate term $-\mathrm{i}\Gamma_n^{\mathrm{imp}}$. For $\Sigma_n^{\mathrm{el}}(E)$, it is desirable that it simultaneously satisfies (i) Fermi-liquid behavior: $\Sigma_n^{\mathrm{el}'}(E) = -\lambda_n^{\mathrm{el}}(E - \mu)$ and $-\Sigma_n^{\mathrm{el}''}(E) \propto (E - \mu)^2 + (\pi k_{\mathrm{B}} T)^2$ for small $E - \mu$[105], (ii) particle-hole symmetry: $\Sigma(E + \mu) = -\overline{\Sigma}(-E + \mu)$, (iii) Kramers-Kronig consistency[6], and (iv) $|E|^{-2}$-decay for large $|E|$ to avoid an ultraviolet divergence[105]. These considerations yield the expression:

$$\frac{\Sigma_n^{\mathrm{el}}(E)}{W_n} = \frac{\lambda_n^{\mathrm{el}}}{\left(1 - \bar{T}_n^2\right)\left(1 + \bar{E}_n^4\right)} \left\{ \bar{E}_n \left[ \bar{T}_n^2 \left(1 + \bar{E}_n^2\right) - \left(1 - \bar{E}_n^2\right) \right] - \mathrm{i}\sqrt{2} \left( \bar{E}_n^2 + \bar{T}_n^2 \right) \right\}, \tag{12}$$

where $\bar{E}_n = (E - \mu)/W_n$ and $\bar{T}_n = \pi k_{\mathrm{B}} T/W_n$ are energy ratios, with $W_n$ an ultraviolet scale that the user must specify (see Supplementary Section S2). The derivation of Eq. (12) is given in Supplementary Section S2, where an alternative expression for $\Sigma_n^{\mathrm{el}}(E)$ (also implemented in xARPES) is provided. The Fermi-liquid behavior imposed on Eq. (12) has relatively wide applicability, since it is obtained for various theoretical models, as well as observed experimentally in several systems, as detailed in Supplementary Section S2.

Finally, we discuss $\Sigma_n^{\mathrm{ph}}(E)$ and its relation to $\alpha^2 F_n(\omega)$. In the problem of Bloch electrons coupled to non-interacting phonons, the finite-temperature perturbation theory in the atomic displacements for the retarded self-energy yields at the lowest order in the reciprocal of the atomic mass, beside

$E$-independent terms contributing to the static self-energy[39,42], the dynamical Fan-Migdal term[37,38,106]:

$$\Sigma_n^{\mathrm{FM}}(E,\mathbf{k}) = \int \frac{\mathrm{d}\mathbf{q}}{\Omega^{\mathrm{BZ}}} \sum_{m\nu\pm} \left|g_{mn\nu}(\mathbf{k},\mathbf{q})\right|^2 \frac{f^{\pm}\left(\varepsilon_m(\mathbf{k}+\mathbf{q})\right) + n\left(\omega_\nu(\mathbf{q})\right)}{E \pm \omega_\nu(\mathbf{q}) - \varepsilon_m(\mathbf{k}+\mathbf{q}) + \mathrm{i}0^+}, \tag{13}$$

where $f^+(\varepsilon) \equiv f(\varepsilon), f^-(\varepsilon) \equiv 1 - f(\varepsilon)$, $n(\omega) \equiv \left[\mathrm{e}^{\omega/(k_\mathrm{B}T)} - 1\right]^{-1}$ is the Bose-Einstein distribution, $\Omega^{\mathrm{BZ}}$ the Brillouin-zone volume, $g_{mn\nu}(\mathbf{k},\mathbf{q})$ is the EPC matrix element between electronic states $\varepsilon_n(\mathbf{k})$ and $\varepsilon_m(\mathbf{k}+\mathbf{q})$ coupled by a phonon of band $\nu$, wavevector $\mathbf{q}$, and energy $\omega_\nu(\mathbf{q})$, while $0^+$ is a positive infinitesimal. Eq. (13) can equivalently be written with the following two expressions:

$$\Sigma_n^{\mathrm{FM}}(E,\mathbf{k}) = \int_0^\infty \mathrm{d}\omega \int_{-\infty}^\infty \mathrm{d}\varepsilon\, \alpha^2F_n(\omega,\varepsilon,\mathbf{k}) \sum_{\pm} \frac{f^{\pm}(\varepsilon) + n(\omega)}{E \pm \omega - \varepsilon + i0^+} \tag{14}$$

$$\alpha^2F_n(\omega,\varepsilon,\mathbf{k}) = \int \frac{\mathrm{d}\mathbf{q}}{\Omega^{\mathrm{BZ}}} \sum_{m\nu} |g_{mn\nu}(\mathbf{k},\mathbf{q})|^2 \delta(\omega - \omega_\nu(\mathbf{q}))\delta(\varepsilon - \varepsilon_m(\mathbf{k}+\mathbf{q})) \tag{15}$$

where we stress that $\omega$ is a vibrational energy, not a frequency. Eq. (14) can also be derived with a definition of $\alpha^2F_n(\omega,\varepsilon,\mathbf{k})$ that contains the full instead of the non-interacting phonon spectral function[3,8,107], which includes a subset of the higher-order terms in the reciprocal atomic mass.

In ARPES experiments, we are mostly interested in $\Sigma_n^{\mathrm{FM}}(E,\mathbf{k})$ when $E$ remains close to $\mu$. The denominator in Eq. (14) shows that the relevant energies $\varepsilon$ are close to $E \pm \omega$. Phonon energies are typically a few tens of meV, which means that the $\varepsilon$ integral in Eq. (14) probes $\alpha^2F_n(\omega,\varepsilon,\mathbf{k})$ within no more than a few hundred meV around $\varepsilon = \mu$. If electronic energy scales are large compared to phonon energies, as occurs when studying photoemission kinks for bands $\varepsilon_n(\mathbf{k})$ that disperse much more steeply than the phonon dispersion $\omega_\nu(\mathbf{q})$, one expects that the variation of $\alpha^2F_n(\omega,\varepsilon,\mathbf{k})$ over the relevant $\varepsilon$ range is weak in comparison with the variation of the energy denominator in Eq. (14). Under these conditions, one can retain the first term of the Taylor expansion of $\alpha^2F_n(\omega,\varepsilon,\mathbf{k})$ around $\varepsilon = \mu$[68]. Similarly, the wavevector dependence is weak if the electrons disperse much more steeply than the phonons, such that $\alpha^2F_n(\omega,\mu,\mathbf{k})$ can be evaluated at the Fermi wavevector $\mathbf{k}_n^{\mathrm{F}}$ of the photoemission kink being analyzed. Finally, contributions to $\Sigma_n^{\mathrm{ph}}(E)$ from higher-order dynamical terms are not captured independently with our formalism, while the $E$-independent terms should be captured in $\varepsilon_n(\mathbf{k})$ during the fitting, leading to $\Sigma_n^{\mathrm{ph}}(E) = \Sigma_n^{\mathrm{FM}}(E)$. These considerations lead to:

$$\Sigma_n^{\mathrm{FM}}(E) = \int_0^\infty \mathrm{d}\omega\, \alpha^2F_n(\omega)K(E,\omega), \tag{16}$$

$$\begin{aligned} K(E,\omega) &= \int_{-\infty}^\infty \mathrm{d}\varepsilon \sum_{\pm} \frac{f^{\pm}(\varepsilon) + n(\omega)}{E \pm \omega - \varepsilon + \mathrm{i}0^+} \\ &= \Psi\left(\tfrac{1}{2} - \mathrm{i}\tfrac{E-\mu-\omega}{2\pi k_\mathrm{B}T}\right) - \Psi\left(\tfrac{1}{2} - \mathrm{i}\tfrac{E-\mu+\omega}{2\pi k_\mathrm{B}T}\right) \\ &\quad -\mathrm{i}\pi[2n(\omega)+1] \end{aligned} \tag{17}$$

where $K(E,\omega)$ is a kernel function[8,108] and $\Psi$ the digamma function. In the limit of infinitely large electronic energy scales over phonon energies and no higher-order terms, the extracted $\alpha^2F_n(\omega)$ may coincide with $\alpha^2F_n(\omega,\mu,\mathbf{k}_n^{\mathrm{F}})$, which we denote as the "Fermi-surface Eliashberg function" as all electronic scales are evaluated at the Fermi surface. When these conditions are not perfectly met, the extracted $\alpha^2F_n(\omega)$ will represent some mixture of $\alpha^2F_n(\omega,\varepsilon,\mathbf{k})$ for different $\varepsilon$ and $\mathbf{k}$, as well as higher-order contributions. The workflow uses the experimentally acquired $\{\widetilde{\Sigma}_n^{\mathrm{FM}}(E_j)\}$ to obtain $\alpha^2F_n(\omega)$ via kernel inversion of Eq. (16) as an estimate of the true $\alpha^2F_n^{\mathrm{true}}(\omega)$. Here, $\alpha^2F_n^{\mathrm{true}}(\omega)$ is the quantity that is recovered from Eq. (16) for of an infinite amount of unbiased data. Subsequently, $\Sigma_n^{\mathrm{FM}}(E)$ is obtained from $\alpha^2F_n(\omega)$ through Eq. (16). However, direct inversion of Eq. (16) can result in negative values[109] or spurious behavior of $\alpha^2F_n(\omega)$ at low/high energies[110]. The function $\alpha^2F_n(\omega)$ should be positive semidefinite for $\omega \in [0, \omega_n^{\max}]$ with $\omega_n^{\max}$ a maximum frequency, while $\alpha^2F_n(\omega)$ is zero outside this interval. This positive semidefiniteness can be encoded as prior knowledge in a regularization term $aS$, where $a$ is a Lagrange multiplier or hyperparameter, and $S$ is the generalized Shannon-Jaynes information entropy[111]:

$$S(\alpha^2F_n, m_n) = \frac{1}{E_{\mathrm{dim}}} \int_0^\infty \mathrm{d}\omega \left[\alpha^2F_n(\omega) - m_n(\omega) - \alpha^2F_n(\omega)\ln\left(\frac{\alpha^2F_n(\omega)}{m_n(\omega)}\right)\right], \tag{18}$$

where $m_n(\omega)$ is a model function of maximum height $h_n$ that encodes the prior knowledge on $\alpha^2F_n(\omega)$. Additional details on $S$ and $m_n(\omega)$ are provided in Supplementary Section S2, where we also provide the definition of the normalized Euclidean distance measure $M(\alpha^2F_1(\omega), \alpha^2F_2(\omega))$ for the comparison of two Eliashberg functions $\alpha^2F_1(\omega)$ and $\alpha^2F_2(\omega)$.

After inclusion of $aS$ as the log-prior, the most probable $\alpha^2F_n(\omega)$ is obtained in the MEM from the maximization of the log-posterior $L + aS$[47]:

$$\alpha^2F_n(\omega) = \mathrm{argmax}_{\alpha^2F_n^\bullet(\omega)}(L + aS), \tag{19}$$

where $L$ is the log-likelihood after rendering the likelihood dimensionless, and $\alpha^2F_n^\bullet(\omega)$ is the argument of the log-posterior optimization. In xARPES, the maximization of Eq. (19) is performed using Bryan's algorithm[89]. Furthermore, $\alpha^2F_n(\omega)$ can be extracted using $\widetilde{\Sigma}_n'(E)$, $-\widetilde{\Sigma}_n''(E)$, or both. While $\alpha^2F_n(\omega)$ is commonly extracted using only $\widetilde{\Sigma}_n'(E)$[15,60], simultaneous incorporation of $-\widetilde{\Sigma}_n''(E)$ may lead to a better extraction. In that case, $L$ becomes:

$$\begin{aligned} L = -\tfrac{1}{2}\sum_{j=1}^{N_J} \Bigg[ &\left(\frac{\Sigma_n'(E_j) - \widetilde{\Sigma}_n'(E_j)}{\sigma_n'(E_j)}\right)^2 + \ln\left(\frac{\sigma_n'(E_j)}{E_{\mathrm{dim}}}\right) \\ &+ \left(\frac{\Sigma_n''(E_j) - \widetilde{\Sigma}_n''(E_j)}{\sigma_n''(E_j)}\right)^2 + \ln\left(\frac{\sigma_n''(E_j)}{E_{\mathrm{dim}}}\right)\Bigg] - N_J\ln(2\pi), \end{aligned} \tag{20}$$

where $\sigma_n'(E_j)$ and $\sigma_n''(E_j)$ are the standard deviations from the MDC fitting of the respective $\widetilde{\Sigma}_n'(E_j)$ and $\widetilde{\Sigma}_n''(E_j)$, whereas $\Sigma_n(E)$ is calculated from Eq. (11), with $\Sigma_n^{\mathrm{ph}}(E)$ determined using Eq. (16). Several approaches exist in the MEM community to determine $a$, including the historic method[47], the classic method[47], and Bryan's method[89]. Recent approaches suggest determining $a$ by a transition from noise fitting to information fitting of the data upon increasing $a$[112].

Interestingly, there is a "tail" or "upturn"[113,114] in $\Sigma_n'(E)$ near $E = \mu$ from the interplay of the FWHM energy resolution $\Delta E$ with a strong decrease in $P(E,\eta)$ through $f(E)$. Consequently, we exclude $\widetilde{\Sigma}_n(E)$ for $\mu - E < \Delta E$ during the inversion of Eq. (16). Furthermore, optimization of $\Sigma_n^{\mathrm{el}}(E)$ and $\Sigma_n^{\mathrm{imp}}(E)$ as described in the Model parameter optimization subsection is only available when the full $\widetilde{\Sigma}_n(E)$ is used in $L$, as $\widetilde{\Sigma}_n'(E)$ by itself was found to give insufficient information to optimize these terms.

Finally, the EPC strength $\lambda_n^{\mathrm{ph}} \equiv -\partial\Sigma_n^{\mathrm{ph}'}(E)/\partial E|_{E=\mu}$ is commonly determined by a linear fit through $\widetilde{\Sigma}_n'(E)$ near the Fermi edge[115]. However, this evaluation inconveniently coincides with the upturn for $E \approx \mu$. We observe that $\alpha^2F_n(\omega)K(E,\omega)$ is continuous over the domain of $\omega$-integration, so that Leibniz' integral rule can be applied. Combining $\lambda_n^{\mathrm{ph}} = -\partial\Sigma_n^{\mathrm{FM}'}(E)/\partial E|_{E=\mu}$ with Eq. (16) then yields:

$$\lambda_n^{\mathrm{ph}} = \frac{1}{2\pi k_\mathrm{B}T} \int_0^\infty \mathrm{d}\omega\alpha^2F_n(\omega)\mathrm{Im}\left[\Psi_1\left(\frac{1}{2} - \frac{\mathrm{i}\omega}{2\pi k_\mathrm{B}T}\right) - \Psi_1\left(\frac{1}{2} + \frac{\mathrm{i}\omega}{2\pi k_\mathrm{B}T}\right)\right], \tag{21}$$

where $\Psi_1$ is the trigamma function. Instead of fitting near the upturn, $\lambda_n^{\mathrm{ph}}$ in xARPES is based on all the $\Sigma_n(E_j)$ for which $\mu - E_j > \Delta E$ through Eq. (21).

We remark that $\lambda_n \equiv -\partial\Sigma_n'(E)/\partial E|_{E=\mu} = \lambda_n^{\mathrm{ph}} + \lambda_n^{\mathrm{el}}$ because $\Sigma_n^{\mathrm{imp}} = -\mathrm{i}\Gamma_n^{\mathrm{imp}}$ is used.

### Model parameter optimization

A key problem in the parameterization of $A_n(E, \mathbf{k})$ is determining the magnitude of $\Sigma_n^{\mathrm{ph}}(E)$, $\Sigma_n^{\mathrm{el}}(E)$, $\Sigma_n^{\mathrm{imp}}(E)$, and the coefficients that represent $\varepsilon_n(\mathbf{k})$. While the KKBF can be used to distinguish between $\varepsilon_n(\mathbf{k})$ and $\Sigma_n(E)$, the decomposition of the latter into its constituents is usually still performed by visual inspection[116] instead of using a quantitative approach. Here, we extend the probabilistic procedure for extracting $\alpha^2F_n(\omega)$ with Bayesian inference to obtain a quantitative procedure for obtaining the model parameters, whose set we denote with $V$. Therefore, $V$ includes $m_n^{\mathrm{b}}$ or $v_n^{\mathrm{F}}$, $k_n^{\mathrm{F}}$, $\Gamma_n^{\mathrm{imp}}$, $\lambda_n^{\mathrm{el}}$, and $h_n$, where inclusion of the latter implies that the shape of $m_n(\omega)$ is considered known, but its height is not.

We denote with $D$ a set of self-energy data, comprising $\{\widetilde{\Sigma}_n'(E)\}$, $\{-\widetilde{\Sigma}_n''(E)\}$, or $\{\widetilde{\Sigma}_n'(E), -\widetilde{\Sigma}_n''(E)\}$. The posterior probability density $p(\alpha^2F_n(\omega)|D, a, m_n(\omega))$ over $\alpha^2F_n(\omega)$ for given $D$, $a$, and model function $m_n(\omega)$ can be expressed as[89,111]:

$$p\left(\alpha^2F_n(\omega)|D, a, m_n(\omega)\right) = \frac{\mathrm{e}^{L+aS}}{Z^S(a)Z^L(D)}, \tag{22}$$

where $Z^S(a)$ and $Z^L(D)$ are normalization factors over the respective $S$ and $L$, and where Eq. (19) is equivalent to maximizing the logarithm of Eq. (22). It may be recognized in Eq. (20) that $L$ is not just a function of $D$, but also a function of $V$. Thus, after realizing that $Z^L(D) \to Z^L(D, V)$, the expression in Eq. (22) may be recognized as $p\left(\alpha^2F_n(\omega)|V, D, a, m_n(\omega)\right)$. Applying Bayes' rule[111] to Eq. (22) then yields:

$$p\left(V|\alpha^2F_n(\omega), D, a, m_n(\omega)\right) = \frac{p\left(\alpha^2F_n(\omega)|V, D, a, m_n(\omega)\right)}{p\left(D, \alpha^2F_n(\omega)\right)}p(V, D), \tag{23}$$

where the evidence $p\left(D, \alpha^2F_n(\omega)\right)$ is a normalization factor that is constant during determination of $p\left(V|\alpha^2F_n(\omega), D, a, m_n(\omega)\right)$, and $p(V, D)$ contains the prior probabilities over $V$ and $D$. Thus, Eq. (23) provides a quantitative criterion to determine the most probable $V$ for a given $\alpha^2F_n(\omega)$. The xARPES code supports uniform probability distributions over $V$ in $p(V, D)$, although different expressions may be implemented in the future, such that previous experimental/theoretical knowledge can be incorporated for subsequent data sets. Iterative optimization of Eqs. (22) and (23) constitutes the outer loop in Fig. 2. First, $\alpha^2F_n(\omega)$ is determined for a given $V$, after which $V$ is determined for the updated $\alpha^2F_n(\omega)$, until the change of $p\left(V|\alpha^2F_n(\omega), D, a, m_n(\omega)\right)$ is below a given threshold, see the Methods section. The Bayesian procedure described here can be generalized to other inversion problems in which the data $D$ themselves depend on unknown parameters $V$.

### Introduction to the model system and use cases

In the following three sections, we showcase the capabilities of xARPES by studying a model system and two use cases. In the Verification using model data subsection, we use artificial data to demonstrate that xARPES recovers 95% overlap of the 95% confidence intervals of $\widetilde{\Sigma}(E)$ with the true $\Sigma(E)$, for an energy resolution $\Delta E \to 0$. We then compare our approach with a frequently used Lorentzian fitting approach[15,52,56,117], which performs increasingly poorly towards higher binding energies. Subsequently, we show that the sharpness of recovered phonon modes is limited by $\Delta E$, and that the optimization loop recovers $k^{\mathrm{F,true}}$, $m^{\mathrm{b,true}}$, $\Gamma^{\mathrm{imp,true}}$, and $\lambda^{\mathrm{true}} = \lambda^{\mathrm{el,true}} + \lambda^{\mathrm{ph,true}}$ within about 5% for realistic values. Finally, we show that $\alpha^2F(\omega)$ converges towards $\alpha^2F^{\mathrm{true}}(\omega)$ with increasing amounts of unbiased data.

The first use case concerns the 2DEL of the $d_{xy}$-derived bands of Nb-doped $TiO_2$-terminated $SrTiO_3$, showcasing extraction with a parabolic $\varepsilon_n(\mathbf{k})$ from experimental data, displaying high similarity between the Eliashberg functions from left/right branches of the inner $d_{xy}$-derived band. We additionally show that omission of $|M_n(\eta)|^2$ matrix elements can change the extracted $\Sigma(E)$ by over a factor of two. The second use case is on Li-doped graphene, showcasing the implementation for a linear $\varepsilon_n(\mathbf{k})$. We provide Jupyter notebooks for the three examples as described in the Code availability section. The $SrTiO_3$ and Li-doped graphene examples are remarkable due to PMEs $|M_n(\eta)|^2$ for which theoretical expressions exist and notably improve on the self-energy fitting. Their importance depends primarily on interplay between experimental geometry, light polarization, and orbital character[26], and has to be evaluated on a case-by-case basis. Users interested in specifying $|M_n(\eta)|^2$ for fitting their data with xARPES may estimate the PMEs from their data with a heuristic approach[58], from tight-binding calculations separately[118] or combined with Wannierization[119], from the so-called scattered-wave approximation[120], or from Lippmann-Schwinger-based simulations[121]. PMEs are also naturally incorporated in one-step photoemission simulations[122], although separating their effects from $A_n(E, \mathbf{k})$ is not always straightforward from such calculations.

### Verification using model data

We analyze an artificial band map with Gaussian noise, $|M_n(\eta)|^2 = 1$, and a parabolic $\varepsilon_n(\mathbf{k})$ to verify our implementation and investigate how noise and energy resolution affect the extraction of $\Sigma_n(E)$ and the reconstruction of $\alpha^2F_n(\omega)$. We perform the self-energy analysis on the left-hand (L) and right-hand (R) branches of a parabolic dispersion, follow up with the extraction of $\alpha^2F_{\mathrm{R}}(\omega)$, and omit the branch index for symmetric quantities. The added noise is the sole source of difference for the extracted quantities. We generate $A(E, \mathbf{k})$ from a single parabolic $\varepsilon(\mathbf{k})$ at $T = 10$ K with a known $\alpha^2F^{\mathrm{true}}(\omega)$ composed of a sum over two peaks with phonon energies $\omega_k \in \{22, 58\}$ meV, broadenings $\rho_k \in \{0.9, 3.5\}$ meV, and matrix elements $g_k^2 \in \{0.6, 1.0\}$ meV computed from:

$$\alpha^2F^{\mathrm{true}}(\omega) = \sum_{k,\pm} g_k^2 \mathrm{Im}\left(\frac{\pm 1}{\omega \pm \omega_k + \mathrm{i}\rho_k}\right). \tag{24}$$

From $\alpha^2F^{\mathrm{true}}(\omega)$, we generate $\Sigma^{\mathrm{ph,true}}(E) = \Sigma^{\mathrm{FM,true}}(E)$ using Eq. (16), to which we add $\Sigma^{\mathrm{el,true}}(E)$ using Eq. (12) while setting $W = E^{\mathrm{F}}$ (the default for parabolic bands), where we define the Fermi energy as $E^{\mathrm{F}} \equiv (\hbar^2k^{\mathrm{F}})^2/(2m^{\mathrm{b}})$, and we add $\Sigma^{\mathrm{imp,true}} = -\mathrm{i}\Gamma^{\mathrm{imp,true}}$. The resulting $\alpha^2F^{\mathrm{true}}(\omega)$ and $\Sigma^{\mathrm{true}}(E)$ are displayed in Fig. 3a. The parabolic dispersion is displaced by $k^{\varepsilon} = 0.1$ Å$^{-1}$, while the values completing the description of $A(E, \mathbf{k})$ constitute the first row of Table 1 and result in $E^{\mathrm{F}} = 150$ meV. We discretize the resulting $A(E, \mathbf{k})$ with $\mathbf{p}(E^{\mathrm{kin}}, \eta)$ parameterized according to Eq. (6) with $N_J = 80$ pairs of data $(\widetilde{\Sigma}_{\mathrm{R}}'(E), -\widetilde{\Sigma}_{\mathrm{R}}''(E))$ for realistic $E^{\mathrm{kin}} \in [29.8, 30.25]$ eV with the photon energy minus the work function $h\nu - \Phi = 30$ eV and 0.02° angular steps for $\eta \in [-6, 10]$°, multiply with an energy-independent $\widetilde{\mathcal{A}}^0 = 10^4$ counts, and set the polynomial terms $\widetilde{B}_0/\widetilde{\mathcal{A}}^0 = 0.2\%$ and $\widetilde{B}_1 = 0$ in Eq (5). Next, we convolve with Gaussian distributions with FWHMs $\Delta E = 2.5$ meV and $\Delta\eta = 0.1$° and add Gaussian noise $\mathcal{N}(\mu^{\mathrm{noise}}, (\sigma^{\mathrm{noise}})^2)$ at each $(E, \eta)$ with $\mu^{\mathrm{noise}}/\widetilde{\mathcal{A}}^0 = 0.2\%$, and noise-to-intensity ratio $\sigma^{\mathrm{noise}}/\widetilde{\mathcal{A}}^0 = 0.025\%$, obtaining the photointensity $P^*(E^{\mathrm{kin}}, \eta)$ displayed in Fig. 3b. We obtain the estimate $h\widehat{\nu} - \widehat{\Phi}$ from the Fermi-edge fitting and compute $P(E, \eta)$. We find $h\widehat{\nu} - \widehat{\Phi} = h\nu - \Phi - (0.06 \pm 0.03)$ meV. Next, we perform the MDC fits using a parabolic $\varepsilon(\mathbf{k})$, showing the fits at a selected binding energy $E^{\mathrm{bin}} = 80$ meV in Fig. 3c, which corresponds to the dashed line in Fig. 3b, and compared to a fit with a linear $\varepsilon(\mathbf{k})$. We find that the quadratic dispersion fits the data better than the linear dispersion.

We remark that the Gaussian noise results in $\chi^2(E_j^{\mathrm{kin}}) = \sum_l^{N_L}\left(P^*(E_j^{\mathrm{kin}}, \eta_l) - \widetilde{P}^*(E_j^{\mathrm{kin}}, \eta_l)\right)^2/(\sigma^{\mathrm{noise}})^2$ with $N_L$ the number of angular data points. For $\Delta E \to 0$, we find the expected $\chi^2(E_j^{\mathrm{kin}}) \approx N_L$ for the parabolic $\varepsilon(\mathbf{k})$, versus $\chi^2(E_j^{\mathrm{kin}}) \approx 7.7\ N_L$ for the linear dispersion, demonstrating that a Lorentzian MDC fitting of $A(E, \mathbf{k})$ yields biased results when the underlying $\varepsilon(\mathbf{k})$ is curved. We temporarily use the true $m^{\mathrm{b}}$ and $k^{\mathrm{F}}$ for the self-energy extraction step to highlight the best possible recovery of $\widetilde{\Sigma}_{\mathrm{L,R}}(E)$ in presence of a finite energy resolution (Fig. 3d) and to evaluate the

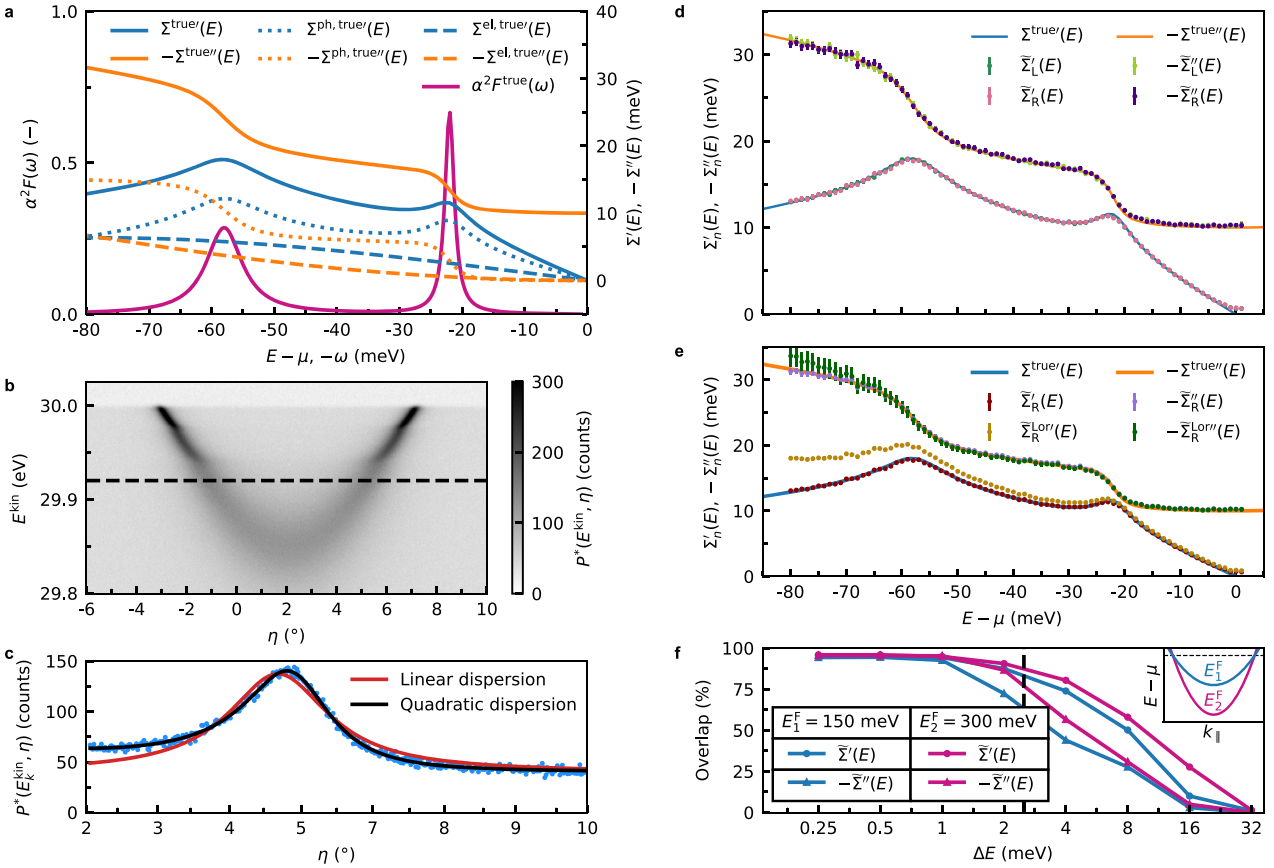


**Fig. 3 | Verification band map and MDC analysis. a** The total real $\Sigma^{\mathrm{true}'}(E)$ (blue) and minus imaginary parts $-\Sigma^{\mathrm{true}''}(E)$ (orange), comprising $\Sigma^{\mathrm{ph,true}'}$ (dotted blue) and $-\Sigma^{\mathrm{ph,true}''}$ (dotted orange) based on $\alpha^2F^{\mathrm{true}}(\omega)$ (magenta), the electron real $\Sigma^{\mathrm{el,true}'}$ (dashed blue) and minus imaginary parts $-\Sigma^{\mathrm{el,true}''}$ (dashed orange), and the impurity term $\Sigma^{\mathrm{imp,true}}(E) = -\mathrm{i}\Gamma^{\mathrm{imp,true}}$ (not shown). **b** Artificial photointensity $P^*(E^{\mathrm{kin}}, \eta)$ for a parabolic dispersion $\varepsilon(\mathbf{k})$ displaced by $k^c = 0.1$ Å$^{-1}$, after adding the energy and angle convolutions, Gaussian noise, and $\Sigma^{\mathrm{true}}(E)$ from **a**. The dashed line corresponds to the selected binding energy $E^{\mathrm{bin}} = 80$ meV in **c**. **c** MDC photointensity $P^*(E_k^{\mathrm{kin}}, \eta)$ (blue dots), fitted with quadratic $\varepsilon(\mathbf{k})$ (black) and linear $\varepsilon(\mathbf{k})$ (red) non-interacting dispersions. **d** Reconstruction of $\Sigma^{\mathrm{true}'}(E)$ (blue) and $-\Sigma^{\mathrm{true}''}(E)$ (orange) for the left-hand $\widetilde{\Sigma}'_{\mathrm{L}}(E)$ (dark green) and $-\widetilde{\Sigma}''_{\mathrm{L}}(E)$ (lime) and the right-hand $\widetilde{\Sigma}'_{\mathrm{R}}(E)$ (pink) and $-\widetilde{\Sigma}''_{\mathrm{R}}(E)$ (indigo). **e** Reconstruction at $\Delta E = 0$ with $\widetilde{\Sigma}'_{\mathrm{R}}(E)$ (maroon) and $-\widetilde{\Sigma}''_{\mathrm{R}}(E)$ (violet) from xARPES, compared to $\widetilde{\Sigma}^{\mathrm{Lor}'}_{\mathrm{R}}(E)$ (gold) and $-\widetilde{\Sigma}^{\mathrm{Lor}''}_{\mathrm{R}}(E)$ (green) from the method described in the text. The confidence intervals of some $\widetilde{\Sigma}'_{\mathrm{L,R}}(E)$ and $\widetilde{\Sigma}^{\mathrm{Lor}'}_{\mathrm{L,R}}(E)$ in **d**–**e** are smaller than the markers. **f** Bands with $E_1^{\mathrm{F}} = 150$ meV (blue) and $E_2^{\mathrm{F}} = 300$ meV (magenta) shown in the inset (different $m^{\mathrm{b}}$ but identical $k^{\mathrm{F}}$), which for a range of energy resolutions $\Delta E$ leads to the displayed overlap of 95% confidence intervals against the energy resolution of $\widetilde{\Sigma}'(E)$ with $\Sigma^{\mathrm{true}'}(E)$ (blue/magenta circles) and $-\widetilde{\Sigma}''(E)$ with $-\Sigma^{\mathrm{true}''}(E)$ (blue/magenta triangles), with the dashed vertical line corresponding to $\Delta E$ used in **a**–**d**.

**Table 1 | True, optimized, and relative differences of parameters for the verification example**

| Parameter | $m_{\mathrm{R}}^{\mathrm{b}}$ ($m_e$) | $k_{\mathrm{R}}^{\mathrm{F}}$ (Å$^{-1}$) | $\Gamma_{\mathrm{R}}^{\mathrm{imp}}$ (meV) | $\lambda_{\mathrm{R}}^{\mathrm{el}}$ (-) | $\lambda_{\mathrm{R}}^{\mathrm{ph}}$ (-) |
|---|---|---|---|---|---|
| True | 1.5875 | 0.25 | 10.0 | 0.12 | 0.28 |
| Opt. | 1.596 | 0.25001 | 10.04 | 0.113 | 0.30 |
| Diff. % | 0.5 | 0.004 | 0.4 | −6 | 7 |

performance of xARPES versus another, commonly used approach (Fig. 3e). At $\Delta E = 2.5$ meV, the left- and right-hand $\widetilde{\Sigma}_{\mathrm{L,R}}(E)$ differ from each other only due to noise, as shown with 95% confidence intervals in Fig. 3d on top of the model $\Sigma(E)$. The finite $\Delta E$ leads to three distinct deviations from $\Sigma^{\mathrm{true}}(E)$. First, $-\widetilde{\Sigma}''(E)$ is overestimated everywhere because a finite $\Delta E$ combined with a dispersive band broadens the MDCs at every $E$. Second, the relatively sharp peak in $\Sigma^{\mathrm{true}'}(E)$ near $E - \mu = -22$ meV cannot be fully recovered. Third, we observe the tail/upturn discussed in the Extraction of the Eliashberg function subsection for $\widetilde{\Sigma}'(E \to \mu)$.

In Fig. 3e, we compare the performance at $\Delta E = 0$ with a commonly used approach that we will call the Lorentzian-based (Lor) method, found in refs. 15,52,56,117. We will refer to the self-energy extracted with this method as $\widetilde{\Sigma}^{\mathrm{Lor}}_n(E)$. Strictly speaking, a linear non-interacting dispersion $\varepsilon_n(\mathbf{k})$ leads to a Lorentzian lineshape in MDC fitting at a given $E_j$, with peak maxima $\widetilde{k}_n(E_j) = \widetilde{r}_n(E_j)\sqrt{2m_eE_j^{\mathrm{kin}}/\hbar^2}$ and FWHMs $\Delta\widetilde{k}_n(E_j)$, as described in Supplementary Section S1. By contrast, if the non-interacting dispersion is curved, fitting MDCs with Lorentzian lineshapes results in biased lineshapes, as was demonstrated in Fig. 3c. The Lorentzian approach inconsistently inserts Lorentzian-based fit parameters into formulae corresponding to a curved $\varepsilon_n(\mathbf{k})$, commonly $\widetilde{\Sigma}^{\mathrm{Lor}'}_n(E_j) = E_j - \mu - \varepsilon_n(\widetilde{k}_n(E_j))$ and $-\widetilde{\Sigma}^{\mathrm{Lor}''}_n(E_j) = (\Delta\widetilde{k}_n(E_j)/2)\partial\varepsilon_n(k_n(E_j))/\partial k$. We compare this approach in Fig. 3e, obtaining 95% overlap of the 95% confidence intervals for the xARPES approach, whereas $\widetilde{\Sigma}^{\mathrm{Lor}}_n(E)$ deviates increasingly from $\widetilde{\Sigma}_n(E)$ towards higher binding energies.

Finally, we quantify the bias originating from a finite energy resolution $\Delta E$ in the extraction of the real and minus imaginary parts of the self-energy data $\widetilde{\Sigma}'(E)$ and $-\widetilde{\Sigma}''(E)$. To do so, we calculate the overlap of the 95% confidence intervals of these data with the respective $\Sigma^{\mathrm{true}'}(E)$ and $-\Sigma^{\mathrm{true}''}(E)$ for energy resolutions ranging from 0.25 meV to 32 meV, and repeat this analysis while changing the Fermi energy (band bottom below $E$

$= \mu$) $E^{\mathrm{F}}$ from 150 meV to 300 meV, based on a different effective mass $m^{\mathrm{b}}$ but the same Fermi wavevector $k^{\mathrm{F}}$. To single out the bias effect, we use the true chemical potential $\mu$ instead of its estimate from the Fermi edge fit described in the Fermi-edge fit subsection. The calculated overlaps are shown in Fig. 3f for bands with Fermi energies $E_1^{\mathrm{F}} = 150$ meV and $E_2^{\mathrm{F}} = 300$ meV shown in the inset. The overlaps converge to 95% for $\Delta E \to 0$, demonstrating that the recovery of $\widetilde{\Sigma}(E)$ is unbiased for the correct choice of the non-interacting dispersion $\varepsilon(\mathbf{k})$. The overlap decreases more rapidly with increasing $\Delta E$ for $-\widetilde{\Sigma}''(E)$ than for $\widetilde{\Sigma}'(E)$ because the energy convolution broadens the MDCs with intensity from adjacent MDCs, an effect that largely cancels out for the peak centers. This broadening effect is further illustrated with the steeper non-interacting band having $E_2^{\mathrm{F}} = 300$ meV, which experiences less broadening and peak shifting upon increasing $\Delta E$. The results in Fig. 3f are invariant to the photointensity noise $\sigma^{\mathrm{noise}}$ as the self-energy confidence intervals increase accordingly until the MDC fitting fails, occurring at $\sigma^{\mathrm{noise}}/\widetilde{\mathcal{A}}^0 = 1.5\%$ for this example.

We now extract the Eliashberg function from the right-hand branch $\alpha^2F_{\mathrm{R}}(\omega)$ and determine the model parameters in the parameter optimization loop: the non-interacting band mass $m_{\mathrm{R}}^{\mathrm{b}}$ and Fermi wavevector $k_{\mathrm{R}}^{\mathrm{F}}$, which together describe the non-interacting dispersion $\varepsilon_{\mathrm{R}}(\mathbf{k})$, the electron-electron coupling coefficient $\lambda_{\mathrm{R}}^{\mathrm{el}}$, the electron-impurity coupling magnitude $\Gamma^{\mathrm{imp}}$, and the height $h_{\mathrm{R}}$ of the model function $m_{\mathrm{R}}(\omega)$. For this artificial example, the code converges to the same maximum for a sufficiently consistent set of initial parameters. As a consequence, we obtain similar results for $\alpha^2F_{\mathrm{L}}(\omega)$, which the user can verify through the Data availability section. We set $W = E^{\mathrm{F}}$ during the optimization, and we initialize $m_{\mathrm{R}}(\omega)$ discretized on 250 evenly spaced energies for $\omega \in [\omega_{\mathrm{R}}^{\min}, \omega_{\mathrm{R}}^{\max}]$ with $\omega_{\mathrm{R}}^{\min} = 1$ meV, $\omega_{\mathrm{R}}^{\max} = 80$ meV, and $h_{\mathrm{R}0} = 0.08$. The parameter ranges provided in Supplementary Tables S1, S2, and S3 indicate for this example how much the parameters can deviate in the respective one-shot, inference loop, and tightly converged cases, without causing the code to fail, while a typical convergence scenario is shown in Supplementary Fig. S1. The resulting $\alpha^2F_{\mathrm{R}}(\omega)$ is shown in Fig. 4a against the known $\alpha^2F^{\mathrm{true}}(\omega)$ together with the extracted $\widetilde{\Sigma}_{\mathrm{R}}(E)$, the reconstructions $\Sigma(E)$ and $\Sigma^{\mathrm{el}}(E)$ calculated from $\alpha^2F_{\mathrm{R}}(\omega)$ via Eq. (24), and $m_{\mathrm{R}}(\omega)$ based on the optimized $h_{\mathrm{R}}$. The reconstructions closely follow the extracted self-energies. In addition, $\Gamma_{\mathrm{R}}^{\mathrm{imp}}$, $k_{\mathrm{R}}^{\mathrm{F}}$, and $m_{\mathrm{R}}^{\mathrm{b}}$ are obtained with high accuracy, as listed in Table 1. By contrast, $\lambda_{\mathrm{R}}^{\mathrm{el}}$ is systematically underestimated, originating from the imposed positive semidefiniteness of $\alpha^2F_{\mathrm{R}}(\omega)$. An unconstrained $\alpha^2F_{\mathrm{R}}(\omega)$ would otherwise contain negative values due to the noise in $\widetilde{\Sigma}_{\mathrm{R}}(E)$. Due to the positive semidefiniteness, $\alpha^2F_{\mathrm{R}}(\omega)$ and $\lambda_{\mathrm{R}}$ are overestimated with respect to $\alpha^2F^{\mathrm{true}}(\omega)$ and $\lambda^{\mathrm{true}}$. We find an increase of 7% from $\lambda^{\mathrm{ph,true}}$ to $\lambda_{\mathrm{R}}^{\mathrm{ph}}$, while $\lambda_{\mathrm{R}}^{\mathrm{tot}}$ only differs from $\lambda^{\mathrm{true}}$ by 3%, emphasizing that the decrease of 6% from $\lambda^{\mathrm{el,true}}$ to $\lambda_{\mathrm{R}}^{\mathrm{el}}$ is a compensation mechanism. Furthermore, $\alpha^2F_{\mathrm{R}}(\omega)$ captures the two peaks from $\alpha^2F^{\mathrm{true}}(\omega)$, although the peak at $\omega = 22$ meV is broadened due to the energy resolution and the somewhat sparsely distributed $\widetilde{\Sigma}(E)$ over the energy range. The peak at $\omega = 58$ meV is slightly broadened as the MEM has less confidence in $\widetilde{\Sigma}_{\mathrm{R}}(E)$ at higher binding energies due to its larger confidence intervals.

To show that the extraction of $\alpha^2F_{\mathrm{R}}(\omega)$ can, in principle, be unbiased, we repeat the extraction for an ideal scenario. In this scenario, we use $N_J = 320$ pairs of data $(\widetilde{\Sigma}_{\mathrm{R}}'(E)_J, -\widetilde{\Sigma}_{\mathrm{R}}''(E))$, energy resolution $\Delta E = 0$, and noise-to-intensity ratio $\sigma^{\mathrm{noise}}/\widetilde{\mathcal{A}}^0 = 0.025\%$. Furthermore, we broaden the first peak of $\alpha^2F^{\mathrm{true}}(\omega)$ modeled with Eq. (24) from $\rho_1 = 0.9$ meV to 2.0 meV, use $h_{\mathrm{R}} = 0.08$ as well as the true model parameters $k^{\mathrm{F,true}}$, $m^{\mathrm{b,true}}$, $\lambda^{\mathrm{el,true}}$, and $\Gamma^{\mathrm{imp,true}}$. The resulting $\alpha^2F_{\mathrm{R}}(\omega)$ and related quantities are displayed in Fig. 4b, showing a complete recovery of $\alpha^2F^{\mathrm{true}}(\omega)$ for a large amount of unbiased data. While these ideal conditions might never be obtained experimentally, the agreement demonstrates convergence toward $\alpha^2F^{\mathrm{true}}(\omega)$ with increasing amounts of unbiased data.

Lastly, we quantify the difference between the input $\alpha^2F_{\mathrm{R}}(\omega)$ and $\alpha^2F^{\mathrm{true}}(\omega)$ for representative laser ($\Delta E = 2.5$ meV) and synchrotron ($\Delta E = 5$ meV) resolutions[33], with noise-to-intensity ratios $\sigma^{\mathrm{noise}}/\widetilde{\mathcal{A}}^0 = 0.025\%$ (used previously for Fig. 3c, with $\widetilde{\mathcal{A}}_n^0$ defined in Eq. (5)) and $\sigma^{\mathrm{noise}}/\widetilde{\mathcal{A}}^0 = 0.05\%$. We calculate minus the information entropy $-S(\alpha^2F^{\mathrm{true}}, \alpha^2F_{\mathrm{R}})$ according to Eq. (18), which represents the extent of surprise in learning $\alpha^2F^{\mathrm{true}}(\omega)$ when already possessing $\alpha^2F_{\mathrm{R}}(\omega)$. Box plots with extrema, quartiles, and medians are shown in Fig. 4c for 50 code executions with random noise for each combination of $(\Delta E, \sigma^{\mathrm{noise}}/\widetilde{\mathcal{A}}^0)$ and $N_J$ pairs of $(\widetilde{\Sigma}_{\mathrm{R}}'(E), -\widetilde{\Sigma}_{\mathrm{R}}''(E))$. We find several trends in the generated Eliashberg functions: spurious peaks and peak-shoulder splittings usually originate from a small amount of $N_J$ for a given phonon energy range, with their effect on $S$ depending on the magnitude of the Eliashberg function. Furthermore, peak magnitudes are governed by the standard deviations $\sigma_n'(E_j)$ and $\sigma_n''(E_j)$ of the respective $\widetilde{\Sigma}_{\mathrm{R}}'(E)$ and $-\widetilde{\Sigma}_{\mathrm{R}}''(E)$. At the smallest $N_J$, the large $-S$ is mostly due to overconfidence of the "chi2kink" method, resulting in overfitting. The curves for $\Delta E = 2.5$ meV at high $N_J$ are illustrative of Fig. 3b, reiterating that $\alpha^2F^{\mathrm{true}}(\omega)$ can be fully recovered for a sufficiently small $\Delta E$ and sufficient $N_J$. For the $\Delta E = 5$ meV cases, $-S$ remains large at higher $N_J$ because the sharp peak in $\alpha^2F^{\mathrm{true}}(\omega)$ is broadened during the MDC fitting. We conclude that inversion of $\alpha^2F_n(\omega)$ is successful

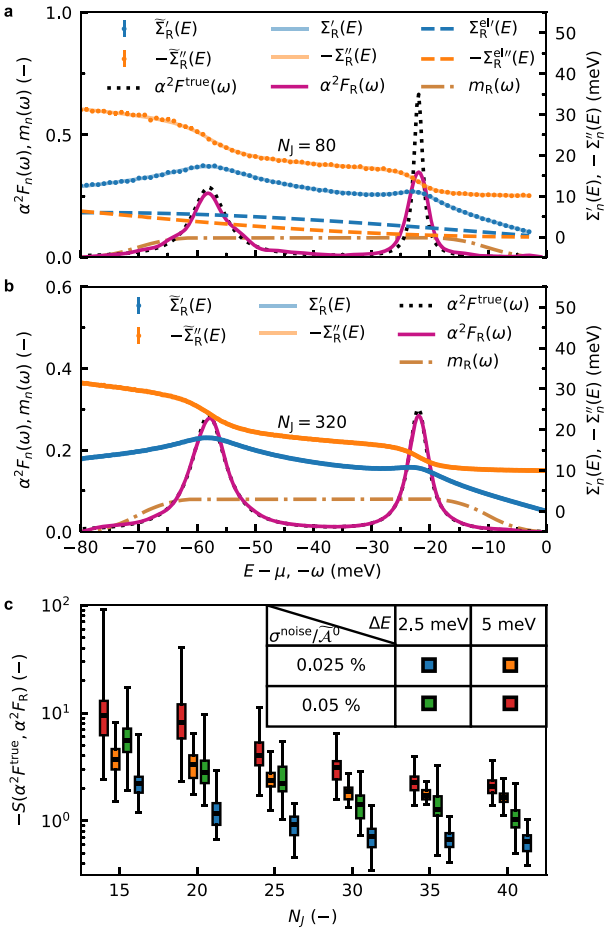


**Fig. 4 | Quantitative analysis of the extraction of $\alpha^2F(\omega)$.** **a** The optimized $\alpha^2F_{\mathrm{R}}(\omega)$ (magenta) versus $\alpha^2F^{\mathrm{true}}(\omega)$ (black dotted) and model function $m_{\mathrm{R}}(\omega)$ (dash-dotted gold), with the real part of the self-energy data $\widetilde{\Sigma}_{\mathrm{R}}'(E)$ (blue bars), the reconstruction $\Sigma_{\mathrm{R}}'(E)$ (blue translucent) and electron contribution $\Sigma_{\mathrm{R}}^{\mathrm{el}'}(E)$ (blue dashed); minus imaginary part of the self-energy data $-\widetilde{\Sigma}_{\mathrm{R}}''(E)$ (orange bars), reconstruction $-\Sigma_{\mathrm{R}}''(E)$ (orange translucent) and electron contribution $-\Sigma_{\mathrm{R}}^{\mathrm{el}''}(E)$ (orange dashed) for the right-hand branch with $N_J = 80$ pairs of data $(\widetilde{\Sigma}_{\mathrm{R}}'(E), -\widetilde{\Sigma}_{\mathrm{R}}''(E))$. **b** The same quantities as in **a** for $N_J = 320$ pairs of data, while using the true model parameters and ideal experimental conditions, as described in the main text. **c** Box plot for minus the information entropy $-S(\alpha^2F^{\mathrm{true}}, \alpha^2F_{\mathrm{R}})$ for combinations of $\Delta E \in \{2.5, 5\}$ meV and noise-to-intensity ratio $\sigma^{\mathrm{noise}}/\widetilde{\mathcal{A}}^0 \in \{0.025, 0.05\}$ %, based on 50 code executions at each combination of $(N_J, \Delta E, \sigma^{\mathrm{noise}}/\widetilde{\mathcal{A}}^0)$.

for sufficiently large amounts of unbiased data, although phonon peaks generally broaden with increasing $\Delta E$, while $\sigma^{\text{noise}}$ increases the variance.

### Photoemission matrix elements in $TiO_2$-terminated $SrTiO_3$

In this first use case, we extract $\Sigma_n(E)$ and $\alpha^2F_n(\omega)$ for a 2DEL of two non-degenerate $d_{xy}$ bands on the $TiO_2$-terminated surface of Nb-doped $SrTiO_3$ along the $k_{[110]}$ direction. In cubic semiconducting $SrTiO_3$, DFPT calculations for the $LO_3$ (longitudinal-optical) and $LO_4$ modes show large long-wavelength coupling ($|g_{mnv}(\mathbf{k}, \mathbf{q} \to \mathbf{0})|$)[123], while cumulant expansion calculations for this system exhibit sidebands displaced from the quasiparticle peak by the $LO_3$ and $LO_4$ energies[124]. Sidebands displaced by the $LO_4$ mode were experimentally observed in several Nb-doped $SrTiO_3$ 2DELs with the Fermi energy $E^F$ comparable to the phonon bandwidth[125–127] (the satellite case[29]), whereas sidebands of the FeSe dispersion displaced by the $LO_3$ and $LO_4$ modes were observed in monolayer FeSe/$SrTiO_3$[128]. Here, we quantify the EPC with $E^F$ larger than the phonon bandwidth (the photoemission kink case[29]), where $\Sigma_n^{\text{ph}}(E)$ shows kinks at $\mu - E$ corresponding to several phonon modes[58].

We consider a 0.7% Nb-doped $SrTiO_3$ sample ($SrTi_{0.993}Nb_{0.007}O_3$) at $T = 20$ K. The other experimental conditions are identical to those listed in the Methods section of ref. 58, and we repeat the PME correction discussed therein. We extract the Eliashberg functions from the inner left (IL) and inner right (IR) branches.

The PMEs of the $d_{xy}$ orbitals of the 2DEL are dependent on the polar emission angle, which we assume to be equal to the detector angle $\eta$ after correcting for the small misalignment in $\phi$ inside Eq. (6). Fortunately, performing the MEC with the physically motivated[58,129] photoemission matrix elements $|M_{d_{xy}}(\eta)|^2 \propto \sin^2(\eta - \phi)$ surrounding the $\bar{\Gamma}_{00}$-point for the $d_{xy}$ bands improves the accuracy of extracted quantities. As in ref. 58, we fit a $\sin^2(\eta - \phi)$ distribution to the energy-integrated photointensity $P(\eta)$, after which we subtract the fitted $\phi = 0.57°$ from the band map to account for detector misalignment. We then determine $\widetilde{\gamma}_n(E)$ and $\widetilde{r}_n(E)$ for the four branches, while manually iterating over $k_n^c$, finding that the zone center displacements and inner/outer (I/O) Fermi vectors, namely $k_n^c = -0.0014$ Å$^{-1}$, $k_I^F = 0.142$ Å$^{-1}$, and $k_O^F = 0.208$ Å$^{-1}$, yield the desired particle-hole symmetry for $\Sigma_n'(E)$ calculated with Eq. (9) simultaneously for all four branches. We preliminarily assign $m_{I,O}^b = 0.6\ m_e$ from visual inspection for the inner (I) and outer (O) bands. The $d_{xy}$ bands together with the MDC maxima along the $k_{[110]}$ direction are shown in Fig. 5a, while $\widetilde{\Sigma}_n'(E)$ and $-\widetilde{\Sigma}_n''(E)$ are shown for all four branches in Supplementary Fig. S2. Next, we perform the optimization loop with an electron-electron scale parameter $W_{IR} = E_{IR}^F = (\hbar k_{IR}^F)^2/(2m_{IR}^b)$ in Eq. (12). The optimization loop yields $m_{IR}^b = 0.59\ m_e$, $k_{IR}^F = 0.141$ Å$^{-1}$, $\Gamma_{IR}^{\text{imp}} = 16.5$ meV, and $\lambda_{IR}^{\text{el}} = 0$, such that $\lambda_{IR}^{\text{el,true}}$ might be too small to be resolved. We calculate $\lambda_{IR}^{\text{ph}} = 0.46$ using Eq. (12), appreciably smaller than the outer branch values $\lambda_{OR}^{\text{ph}} = 0.63$ and $\lambda_{OL}^{\text{ph}} = 0.68$ from ref. 58. The $TO_4$ and $LO_4$ modes[130] found previously in $\alpha^2F_{IR}(\omega)$[58] at $\omega_{TO_4} = 69$ meV and $\omega_{LO_4} = 84$ meV are also observed in our $\alpha^2F_{IR}(\omega)$ within approximately 2 meV. By contrast, the previously observed $\omega_{LO_3} = 56$ meV now appears as a shoulder, while the large feature near 40 meV has been red-shifted towards 30 meV. Furthermore, $\alpha^2F_{IR}(\omega)$ is resolved with less detail compared to those in ref. 58, primarily because the current data have been sampled for fewer $\eta$-values. Our $LO_4$ mode is red-shifted by approximately 8 meV compared to the DFPT calculations of ref. 131, potentially due to accumulated charges[132] from the in-gap states[133] and from the 2DEL.

We calculate the Euclidean distance measure provided in Supplementary Section S2 as $M(\alpha^2F_L(\omega), \alpha^2F_R(\omega)) = 0.0099$. The high similarity raises the question whether $\alpha^2F_{IL}^{\text{true}}(\omega)$ and $\alpha^2F_{IR}^{\text{true}}(\omega)$ should be identical. The Fermi surface of the $TiO_2$-termination suggests that the band structure still has the $C_4$-symmetry obtained by terminating tetragonal $SrTiO_3$ along the [001]-direction. However, previously measured spin components for the $d_{xy}$-derived bands find a small difference in the $z$-component[134], potentially affecting the spin dependence of the Eliashberg function[135]. Future first-principles calculations and experiments on the Eliashberg functions and the spin texture of the 2DEL on $SrTiO_3$ might elucidate if the underlying quantities are identical indeed.

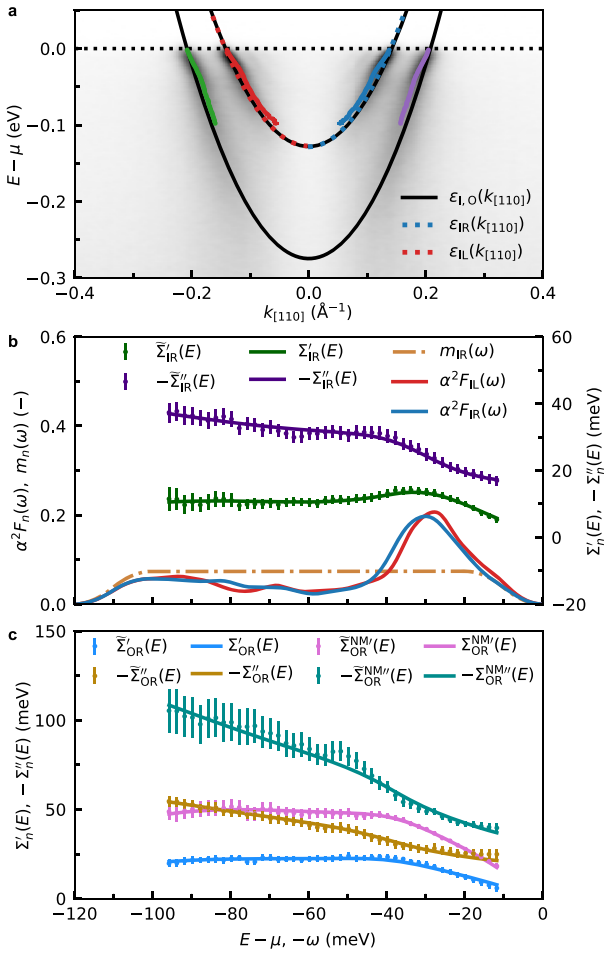


**Fig. 5 | Self-energy and Eliashberg function of $SrTiO_3$. a** Band map of the 2DEL on the $TiO_2$-terminated surface of $SrTiO_3$ along $k_{[110]}$, showing MDC maxima with 95% confidence intervals for the outer left (green), inner left (red), inner right (blue), and outer right (purple) branches, with inner/outer bands (black) from initial guesses and the optimized inner left/right branches (dashed red/blue). **b** Comparison of the inner left $\alpha^2F_{IL}(\omega)$ (red) with the inner right $\alpha^2F_{IR}(\omega)$ (blue) with the optimized model function $m_{IR}(\omega)$ (dash-dotted gold), based on the inner right real $\widetilde{\Sigma}_{IR}'(E)$ (green bars) and minus imaginary data $-\widetilde{\Sigma}_{IR}''(E)$ (indigo bars), with reconstructions $\Sigma_{IR}'(E)$ (blue) and $-\Sigma_{IR}''(E)$ (indigo). **c** Self-energies of the outer right branch obtained with and without (NM) photoemission matrix elements, comprising the corrected real $\Sigma_{OR}'(E)$ (light blue) and imaginary parts $-\Sigma_{OR}''(E)$ (gold), and the real $\Sigma_{OR}^{NM\prime}(E)$ (pink) and imaginary parts $-\Sigma_{OR}^{NM\prime\prime}(E)$ (teal) without the correction. Corresponding data are denoted using a tilde.

Finally, we investigate the effect of the PMEs by comparing the self-energies after the optimization loop for the xARPES approach for the outer right (OR) branch versus omitting the PMEs (NM for "no MEC") during the MDC fitting. We choose the OR branch as $-\widetilde{\Sigma}_{IL}^{\text{ph,NM}\prime\prime}(E)$ and $-\widetilde{\Sigma}_{IR}^{\text{ph,NM}\prime\prime}(E)$ contain negative values after running the optimization loop, which is unphysical. Figure 5c shows the self-energies and reconstructions with and without the MEC, with $\Sigma_{OR}^{NM}(E)$ being approximately twice as large as $\Sigma_{OR}(E)$, primarily because the optimization loop assigns a small $m_{OR}^{b,NM} = 0.46\ m_e$ versus $m_{OR}^b = 0.59\ m_e$ for a good simultaneous fitting of $\Sigma_{OR}^{NM\prime}(E)$ and $-\Sigma_{OR}^{NM\prime\prime}(E)$ (compare Eqs. (9)–(10)). By contrast, $\Sigma_{OR}'(E)$ and $-\Sigma_{OR}''(E)$ from the fit with the MEC agree well with the respective data $\widetilde{\Sigma}_{OR}'(E)$ and $-\widetilde{\Sigma}_{OR}''(E)$, and closely resemble those of ref. 58. In agreement with ref. 58, we

also obtain $\lambda_{\mathrm{OR}}^{\mathrm{el}} = 0 = \lambda_{\mathrm{OR}}^{\mathrm{el,NM}}$. Finding that $\Sigma(E)$ can be over twice as large when neglecting the MEC, we conclude that the MEC can be essential for reducing bias in extracted quantities.

### Eliashberg-function similarity in quasi-freestanding graphene

The data were provided by the authors of ref. 54 and are shown as cut #2 in Fig. 7b of ref. 54. Bands of the Dirac cones surrounding K-points are approximately linear[136], such that we fit them with the linear $\varepsilon_{\mathrm{L,R}}(\mathbf{k})$ fitting procedure of xARPES described in Supplementary Section S1. The geometry of the setup is obtained by performing a 90° rotation of the detector around the $z$-axis—aligning the detector slit along the $y$-axis—followed by a positive $\phi$-rotation that results in the finite $k_x$. We follow ref. 54 in employing a "small-angle approximation"[137], resulting in $k_y = p_y \approx |\mathbf{p}| \sin(\theta + \eta)$, followed by correcting for misalignment with $\theta = -2.28°$. In ref. 54, the data from the two kinks were combined into one pair of real and minus imaginary parts by a method that we describe in Supplementary Section S5, followed by the extraction of a single Eliashberg function. Instead, we separately extract $\Sigma_{\mathrm{L}}(E)$, $\alpha^2F_{\mathrm{L}}(\omega)$, $\Sigma_{\mathrm{R}}(E)$, and $\alpha^2F_{\mathrm{R}}(\omega)$, and discuss the symmetries that relate them to one another. A linear dispersion can be described by two non-interacting band parameters: the Fermi velocity $v_n^{\mathrm{F}}$ and Fermi wavevector $k_n^{\mathrm{F}}$. Since two parameters can be eliminated during the MDC fitting, all model parameters with a linearized band can be quantified in the optimization loop.

Prior DFPT calculations of the decay rate in graphene display two large peaks near $\omega$ = 160 meV and $\omega$ = 195 meV[138], arising largely from the in-plane $A_1'$ mode at the K-point and the in-plane $E_{2g}$ mode at the Γ-point[139], respectively. Charge dopants red-shift these modes, bring them closer together, increase the relative intensity of the $A_1'$-based mode, and introduce additional spectral weight in $\alpha^2F_n(\omega)$ below $\omega$ = 100 meV from out-of-plane coupling of the C-atoms with dopants[140].

Using $\Delta E$ = 10 meV[54], we perform the Fermi-edge correction described in the Fermi-edge fit subsection, finding the best fit for $T$ = 50 K, which we assign as the sample temperature. Next, we fit the MDCs on an interval $\mu - E \in [0, 246]$ meV to capture the $E_{2g}$ and $A_1'$ contributions. We use the MEC from ref. 54 with its details discussed in Supplementary Section S5. Afterwards, we perform the optimization loop for the left-hand and right-hand sides using $W_{\mathrm{L,R}}$ = 1.5 eV in Eq. (12), equal to the binding energy of the Dirac crossing. The MDC maxima and optimized non-interacting dispersions are displayed in Fig. 6a, based on $v_{\mathrm{L}}^{\mathrm{F}} = -2.67$ eV Å/$\hbar$, and $k_{\mathrm{L}}^{\mathrm{F}} = -0.354$ Å$^{-1}$, $v_{\mathrm{R}}^{\mathrm{F}} = 2.85$ eV Å/$\hbar$, and $k_{\mathrm{R}}^{\mathrm{F}} = 0.358$ Å$^{-1}$. Figure 6b displays the extracted $\widetilde{\Sigma}_{\mathrm{R}}(E)$ and reconstructed $\Sigma_{\mathrm{R}}(E)$, as well as $\alpha^2F_{\mathrm{L}}(\omega)$ compared to $\alpha^2F_{\mathrm{R}}(\omega)$ displayed together with its optimized $m_{\mathrm{R}}(\omega)$. The complete set of $\widetilde{\Sigma}_{\mathrm{L}}(E)$ and $\Sigma_{\mathrm{L}}(E)$ is provided in Supplementary Section S5. We calculate $\lambda_{\mathrm{L}}^{\mathrm{ph}} = 0.48$ and $\lambda_{\mathrm{R}}^{\mathrm{ph}} = 0.53$, with most of the discrepancy potentially originating from experimental asymmetry. A large peak at $\omega$ = 166 meV can be observed in $\alpha^2F_{\mathrm{R}}(\omega)$, likely incorporating the $E_{2g}$ and $A_1'$ contributions. These peaks are red-shifted by $\omega$ = 10 meV in DFPT calculations of the isotropic $\alpha^2F(\omega)$ in Li-doped graphene[140], where absence of the substrate and intercalation compounds might contribute to the discrepancy. Some spectral weight can be observed in $\alpha^2F_{\mathrm{R}}(\omega)$ near $\omega$ = 35 meV and $\omega$ = 85 meV, reflecting the low-frequency spectrum found in the DFPT calculations[140]. The optimization also yields $\Gamma_{\mathrm{L}}^{\mathrm{imp}} = 115.6$ meV, $\Gamma_{\mathrm{R}}^{\mathrm{imp}} = 120.9$ meV, and $\lambda_{\mathrm{L}}^{\mathrm{el}} = 0 = \lambda_{\mathrm{R}}^{\mathrm{el}}$. Introduction of curvature in the non-interacting dispersion—with the center wavevector $k_n^{\mathrm{c}}$ determined by the KKBF—did not lead to a finite $\lambda_n^{\mathrm{el}}$ or other appreciably different results. While calculations for doped graphene in the random-phase approximation (RPA) predict a plasmon contribution in $-\Sigma_n^{\mathrm{el}''}(E)$ of the order of 100 meV as $E - \mu$ approaches the Dirac point[141–143], our results suggest that $\Sigma_n^{\mathrm{el}}(E)$ is weak for binding energies up to the phonon bandwidth. However, while $\Sigma_n^{\mathrm{el}}(E)$ in Eq. (12) may be related to coupling with particle-hole excitations in the RPA for a parabolic $\varepsilon_n(\mathbf{k})$ as described in Supplementary Section S2, its functional form should be different for approximately linear $\varepsilon_n(\mathbf{k})$[141]. Moreover, Eq. (12) does not include coupling with plasmons, rendering it increasingly unsuitable to describe electron-electron interactions in doped graphene towards higher binding energies.

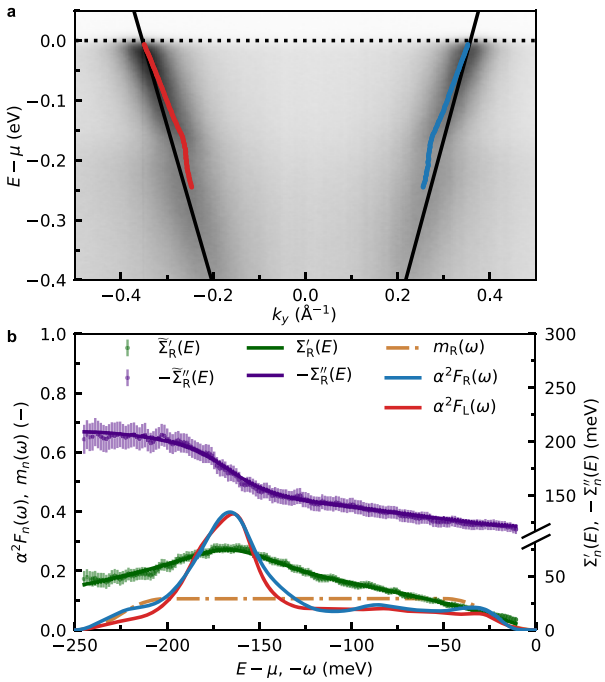


**Fig. 6 | Self-energy and Eliashberg function of Li-doped graphene. a** Band map of Li-doped graphene along cut #2 from ref. 54 with two optimized linear bands, as well as the left-hand (L, blue) and right-hand (R, red) MDC maxima with 95% confidence intervals. **b** Comparison of $\alpha^2F_{\mathrm{L}}(\omega)$ (red) against $\alpha^2F_{\mathrm{R}}(\omega)$ (blue), with optimized model function $m_{\mathrm{R}}(\omega)$ (dash-dotted gold), based on the right-hand real $\widetilde{\Sigma}_{\mathrm{R}}'(E)$ (green bars) and minus imaginary data $-\widetilde{\Sigma}_{\mathrm{R}}''(E)$ (indigo bars), with reconstructions $\Sigma_{\mathrm{R}}'(E)$ (green) and $-\Sigma_{\mathrm{R}}'(E)$ (indigo).

We observe good agreement between $\alpha^2F_{\mathrm{L}}(\omega)$ and $\alpha^2F_{\mathrm{R}}(\omega)$, obtaining the large peak in the latter at $\omega$ = 164 meV, consistent with verification for large $N_f$ found in the Verification using model data subsection. The weaker resolution of the phonon modes in $\widetilde{\Sigma}_{\mathrm{L}}(E)$ reflects lower confidence of the MEM in the left-hand data. The Euclidean distance measure between the two Eliashberg functions is $M(\alpha^2F_{\mathrm{L}}(\omega), \alpha^2F_{\mathrm{R}}(\omega)) = 0.0067$. This Euclidean distance is lower than $M(\alpha^2F_{\mathrm{L}}(\omega), \alpha^2F_{\mathrm{R}}(\omega)) = 0.0099$ obtained for the $SrTiO_3$ in the Photoemission matrix elements in $TiO_2$-terminated $SrTiO_3$ subsection and much lower than the distance between two previously compared experimental Eliashberg functions[144], suggesting that the agreement for the Li-doped graphene is unprecedented. As with the $SrTiO_3$, this high similarity between $\alpha^2F_{\mathrm{L}}(\omega)$ and $\alpha^2F_{\mathrm{R}}(\omega)$ suggests that the underlying $\alpha^2F_{\mathrm{R}}^{\mathrm{true}}(\omega)$ and $\alpha^2F_{\mathrm{L}}^{\mathrm{true}}(\omega)$ may be identical. The two kinks are given by two $\pm k_y$ components perpendicular to the Γ − K high-symmetry line, which in monolayer graphene are related by a $C_2$ axis and a $\sigma_d$ plane[145]. The Si/Co(0001) subsystem (see Fig. 3 of ref. 54) breaks the $\sigma_d$ plane symmetry, whereas the introduction of Si/Co(0001) and Li intercalation both break the $C_2$ symmetry. However, the Li/graphene subsystem is often regarded as quasi-freestanding[54], which would still preserve the $\sigma_d$ symmetry. Although a spin splitting between the sublattices of doped graphene could also break the symmetry along the Γ − K-path via spin dependence of the Eliashberg function[135], this degree of freedom should not be important as the magnetization in the graphene sheet was found to be negligible[54]. Therefore, we expect that the asymmetry of the experimental setup might be the main cause of the observed difference between $\alpha^2F_{\mathrm{L}}(\omega)$ and $\alpha^2F_{\mathrm{R}}(\omega)$, as the underlying functions should be identical based on the symmetry. Interestingly, the omission of the Fermi-edge correction for linearized bands leads to a much larger $M(\alpha^2F_{\mathrm{L}}(\omega), \alpha^2F_{\mathrm{R}}(\omega)) = 0.022$, with $\alpha^2F_{\mathrm{L}}(\omega)$ and $\alpha^2F_{\mathrm{R}}(\omega)$ obtained without the edge correction shown in Supplementary Fig. S3. This increase of $M(\alpha^2F_{\mathrm{L}}(\omega), \alpha^2F_{\mathrm{R}}(\omega))$ of over a factor of three shows that

experimental factors can lead to large differences in extracted self-energies and Eliashberg functions.

## Discussion

We have introduced rigorous and quantitative approaches for extracting many-body properties from angle-resolved photoemission band maps. We make our methodologies available to the scientific community through the first release of xARPES, a GPLv3-licensed Python package. This initial release focuses on the analysis of dispersion kinks arising from electron-phonon interactions. Two of its building blocks are based on the current state of the art. Starting from raw experimental data, the code first quantifies the band map data via non-interacting dispersions and causal self-energies, with the user specifying the number of dispersions, the self-energies, and the values for parameterizing them, optionally complemented with a photoemission matrix element. Second, it decomposes the self-energy into impurity, electron-electron, and electron-phonon contributions, concurrently extracting the electron-phonon Eliashberg coupling function (Fig. 3).

xARPES complements existing codes for angle-resolved photoemission analysis—which are usually tied to a beamline and excel at data visualization—with novel and powerful functionalities for many-body analysis. Concerning the self-energy extraction, we show that traditional Lorentzian fitting of momentum-distribution curves, suitable for linear dispersions[31], introduces bias when applied to curved dispersions. The present approach improves on the extraction by fitting curved dispersions, which has been implemented in xARPES for parabolic bands. Furthermore, we introduce the possibility of specifying the photoemission matrix element during the fitting process. Existing methods for extraction of the Eliashberg function with the maximum-entropy method usually rely on manual assignment of the parameters governing the non-interacting dispersion and individual scattering channels. By contrast, the extraction is wrapped inside a bilevel optimization, using a newly derived criterion based on Bayesian inference for determining the most probable model parameters. This framework is designed to eliminate tedious and arbitrary manual parameter optimization, resulting in a robust and reproducible platform that is well-suited for objective comparisons between different datasets. We illustrate this by extracting and comparing Eliashberg functions from two symmetry-equivalent kinks within the same photoemission band map (Fig. 6).

We have extensively verified and validated the performance to demonstrate the potential of the present analysis. The robustness of the maximum-entropy-based Bayesian inference is confirmed using synthetic data with added noise and energy resolution as input. We show that the model parameters are accurately recovered, with precision converging monotonically to the exact result as energy resolution improves, the signal-to-noise ratio increases, and the data sampling becomes finer (Figs. 3–4).

Using a case where the quadratic dispersion is indispensable, we analyze photoemission kinks from the 2-dimensional electron liquid on $TiO_2$-terminated $SrTiO_3$ (Fig. 5a). We achieve good agreement between the Eliashberg functions extracted from both sides of the parabolic band. Furthermore, we demonstrate that omission of the photoemission matrix element can modify the results by over a factor of two (Fig. 5b). We also apply our approach to published data on Li-doped graphene[54], showcasing the applicability of linearized non-interacting dispersions in xARPES. Here, a comparison of the Eliashberg functions extracted from two different kinks of a band map shows that Li-doped graphene is an excellent platform for future benchmarking of the extraction procedure (Fig. 6). With the advent of ever-improving experimental equipment, we introduce an Euclidean distance measure to compare Eliashberg functions that are believed to be identical, either via symmetry or from one experiment to the next.

The development of the present formalism was driven by the need for a platform to accurately compare experimentally extracted electron spectral functions with first-principles calculations in the presence of many-body interactions, particularly electron-phonon coupling. Achieving this long-term objective requires a standardized method for extracting the Eliashberg function from photoemission measurements. Like other ARPES-based approaches, xARPES extracts an Eliashberg function that depends only on the band, its location in reciprocal space, and on the exchanged phonon energy. However, in fundamental theory, this function also depends on the initial energy and momentum of the electron[3]. We have shown under which conditions the experimentally extracted Eliashberg function can be compared with its theoretical counterpart, usually evaluated at the chemical potential and Fermi momentum relevant to the experimental conditions[68,108]. In the future, xARPES may be expanded to compare the non-interacting dispersion calculated from theoretical methods with its experimental counterpart, as well as for comparing the self-energy evaluated on the renormalized dispersion. As a first step in this direction, in Supplementary Fig. S4, we have fitted the mass of the non-interacting dispersion to Kohn-Sham eigenvalues of the bottom of the zone-center surface state on the surface of Al(001) calculated with ABINIT[69,74,146], followed by extracting the self-energies and the Eliashberg function with this fixed non-interacting band mass for a band map published in ref. 147. The relevant parameters of this fitting procedure are provided in Supplementary Table S4. The modular structure of xARPES supports future development, extension, and potential interfacing with existing codes for analyzing angle-resolved photoemission spectroscopy. With respect to the underlying physical model, we foresee three main avenues for evolution. First, implementing higher-order polynomial forms of the dispersion would improve accuracy in cases where linear or quadratic models fall short. Second, incorporating higher-order phonon processes could be pursued, for example, through self-consistent calculations at the self-energy level[148] or via the cumulant expansion applied directly to the spectral function[149]. Third, the library of Kramers-Kronig-consistent phenomenological models for the electron-electron self-energy, currently limited to Fermi-liquid forms, could be expanded to capture a wider range of behaviors found in quantum materials, such as marginal Fermi liquids[150] or systems with strong plasmon coupling[151]. On the implementation side, the current method relies on fitting isolated momentum-distribution curves, which do not account for the finite energy resolution. A natural next step would be a code that analyzes the full two-dimensional photoemission intensity while incorporating the effects of energy resolution, by directly extracting the Eliashberg function from the photointensity[89]. Additional enhancements could broaden the user base and improve usability. These include support for multiple experimental file formats, support for different experimental geometries, and interfaces with existing codes that specialize in data visualization.

The integration of machine learning could accelerate various tasks of the formalism. One such option is the automatic selection of the energy and momentum windows for the fitting. Ultimately, the current optimization loop could be replaced by an artificial neural network that directly optimizes all the model parameters. Meanwhile, the standardized extraction approach presented here can be used to procure harmonized training data for the supervised learning of these future machine learning models.

With the release of xARPES, we aim to foster a collaborative effort between the photoemission and first-principles communities to establish shared standards that enable unbiased comparisons between first-principles many-body theories and experimental data, thereby driving progress on both theoretical and experimental fronts.

## Methods

### Technical details of the xARPES code

The code is object-oriented, allowing the user to manipulate data through objects such as the `BandMap` class. It can be executed in Jupyter notebooks or with regular Python files, requiring Python version 3.10 or higher. Fitting of momentum-distribution curves is wrapped around the Python fitting package LMFIT[152], allowing the specification of the number of bands. The Bayesian inference loop employs `scipy.optimize.minimize`[153], so that the user can choose different optimization algorithms. On a 12th Gen Intel(R) Core(TM) i7-1255U 2.60 GHz CPU, individual code blocks from Fig. 2 typically complete within one second. The Bayesian inference loop wrapping the MEM can take several minutes to complete, depending on the

initial guess and the size of the singular space controlled with the cutoff value $\sigma_n^{\mathrm{cut}}$ in Bryan's algorithm[89]. xARPES can currently load band maps from NumPy arrays and from the IGOR Pro binary wave format (`.ibw`). The band map needs to have the detector angle on the abscissa and the kinetic energy on the ordinate, while the user must provide the angular resolution and the sample temperature. The energy resolution must be provided by the user if the chemical potential has to be determined from the Fermi edge fitting.

### Maximum-entropy method in xARPES

Within the MEM, xARPES uses the so-called "chi2kink" method[112] to determine the hyperparameter/Lagrange multiplier $a$. With this method, $\chi^2$ is defined as the sum of the squared terms in Eq. (20), followed by fitting $\log_{10}[\chi^2(\log_{10}(a))]$ with the following function:

$$\phi(x; g, b, c, d) = g + \frac{b}{1 + \mathrm{e}^{-d(x-c)}}. \tag{25}$$

Once the fitting has been completed, $a$ is obtained from $a = 10^{c - f^{\chi^2}/d}$ with a tuning parameter $f^{\chi^2} \in [2, 2.5]$[112]. The default values in xARPES are $f^{\chi^2} = 2.5$ when fitting with both $\widetilde{\Sigma}_n'(E)$ and $-\widetilde{\Sigma}_n''(E)$, contrasting $f^{\chi^2} = 2.0$ when fitting just one of them (commonly $\widetilde{\Sigma}_n'(E)$). In practice, users must provide a chi2kink range minimum $\log_{10}(a_n^{\mathrm{min}})$ and a maximum $\log_{10}(a_n^{\mathrm{max}})$, and check that the kink in $\chi^2$ is correctly fitted within this interval, after which $\alpha^2 F_n(\omega)$ is determined in a final iteration from the fitted $a$. The default parameters are $\sigma_n^{\mathrm{cut}} = 1$ for the initial one-shot calculation and the optimization loop versus $\sigma_n^{\mathrm{cut}} = 10^{-4}$ for a final extraction; $\log_{10}(a_{\mathrm{n}}^{\mathrm{min}}) = 3$ for the initial calculation and optimization, versus $\log_{10}(a_{\mathrm{n}}^{\mathrm{min}}) = 1$ during the final extraction, with $\log_{10}(a_{\mathrm{n}}^{\mathrm{max}}) = \log_{10}(a_{\mathrm{n}}^{\mathrm{min}}) + 8$ in all cases. The Eliashberg function extraction employs Bryan's algorithm[89] with a default convergence threshold $t = 10^{-8}$.

### Fermi-edge fit

During the band map analysis for a fixed photon energy $h\nu$ and polarization $\boldsymbol{\epsilon}$, it is beneficial to have the photointensity as a function of the electron energy $E - \mu$, which is written as $P(E, \eta)$ in Eq. (4). Here, we outline how $P(E, \eta)$ can be obtained, and highlight possible sources of bias in establishing the relation between $E$ and $E^{\mathrm{kin}}$. Integration over the momentum results in the angle-integrated photointensity:

$$P(E) \propto \int_{-\infty}^{\infty} \mathrm{d}E' R(E - E') D(E'), \tag{26}$$

where we define the shorthand notation $D(E) \equiv B(E) + f(E)\sum_n |M_n(E)|^2 A_n(E)$. However, for a given work function $\Phi$, the energy measured by the detector is $E^{\mathrm{kin}}$, yielding:

$$P^*(E^{\mathrm{kin}}) \propto \int_{-\infty}^{\infty} \mathrm{d}E^{\mathrm{kin}\prime} R(E^{\mathrm{kin}} - E^{\mathrm{kin}\prime}) D(E^{\mathrm{kin}\prime} - h\nu + \Phi + \mu). \tag{27}$$

Thus, to go from the experimentally detected $E^{\mathrm{kin}} = h\nu - \Phi + E - \mu$ to the binding energy coordinate $E - \mu$ requires estimating $h\nu - \Phi$. This can be done through the so-called *Fermi-edge fit*[154], where a profile containing the Fermi-Dirac distribution is fitted to $P^*(E^{\mathrm{kin}})$ to yield the estimate $\widehat{h\nu} - \widehat{\Phi}$, with the hat (^) denoting estimates. Furthermore, the Fermi-edge fit can be used to determine the energy resolution of an experimental setup for a known electronic temperature, or vice versa. In xARPES, the user has to provide these two quantities, while $P^*(E^{\mathrm{kin}})$ is fitted with parameters $A$, $B$, and $C$ for a function of the following form:

$$P^*(E^{\mathrm{kin}}) = \int_{-\infty}^{\infty} \mathrm{d}E^{\mathrm{kin}\prime} R(E^{\mathrm{kin}} - E^{\mathrm{kin}\prime}) \left[ \frac{A}{\mathrm{e}^{(E^{\mathrm{kin}\prime} - C)/(k_{\mathrm{B}}T)} + 1} + B \right], \tag{28}$$

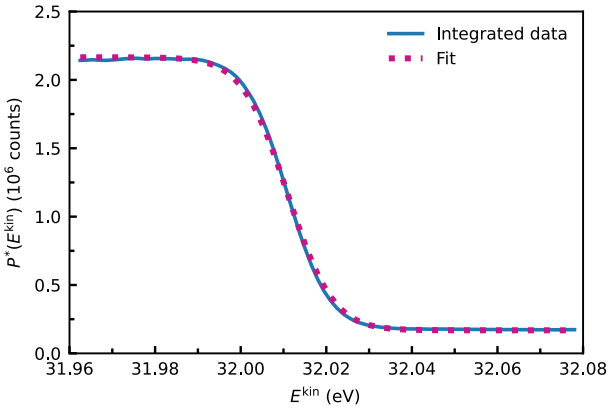


**Fig. 7 | Fermi-edge fit of graphene.** Photointensity $P^*(E^{\mathrm{kin}})$ for Li-doped graphene versus the kinetic energy $E^{\mathrm{kin}}$. The angle-integrated data (blue) and its corresponding fit (magenta).

resulting in $C = \widehat{h\nu} - \widehat{\Phi}$. As an example, we show in Fig. 7 the Fermi-edge fit for the Li-doped graphene from the Eliashberg-function similarity in quasi-freestanding graphene subsection. Afterwards, $\widehat{h\nu} - \widehat{\Phi}$ can be subtracted from $E^{\mathrm{kin}}$ to obtain $\widehat{E} - \widehat{\mu} = E^{\mathrm{kin}} - \widehat{h\nu} - \widehat{\Phi}$, yielding $P$ as a function of $\widehat{E} - \widehat{\mu}$ from Eq. (26). We subsequently write these quantities as $E - \mu$ and $P(E)$, although it should be kept in mind that this coordinate transformation involves an estimate.

We note that $\widehat{h\nu} - \widehat{\Phi}$ is often established before an experiment, for instance from Cu or Au references[154], especially for samples with a poorly resolved Fermi edge or a Fermi edge lying inside an energy gap, which can be the case for insulators, superconductors, and sometimes charge-density waves. Notably, neglecting the dispersion $\varepsilon_n(\mathbf{k})$, the many-body features in $A_n(E, \mathbf{k})$, or $|M_n(E, \eta; h\nu, \boldsymbol{\epsilon})|^2$ may result in a biased estimate $\widehat{h\nu} - \widehat{\Phi}$. The DOS from 1D, 2D, or 3D parabolic dispersion relations projected onto the single momentum dimension of a band map is proportional to $1/\sqrt{E_n^{\mathrm{F}} - (\mu - E)}$, with $E_n^{\mathrm{F}}$ the Fermi energy of a branch $n$. The absence of this factor in Fermi-edge fits leads to bias in $\widehat{h\nu} - \widehat{\Phi}$, even with the commonly used amorphous Au and Cu standards. Furthermore, it is the largest source of bias in the fit from the artificial example in the Verification using model data subsection. Different photoelectric responses between a reference material and the experimental sample can lead to a different $\Phi$, acting as another potential source of bias in $\widehat{E} - \widehat{\mu}$. The case of graphene from Fig. 7 is ideal as its 1D-projected DOS is constant, while its many-body and matrix-element features are weak, leading to a precise and accurate fit. Aside from yielding $\widehat{h\nu} - \widehat{\Phi}$, the Fermi-edge fitting can be used to determine $\widehat{\mu} = \widehat{\Phi}$ within the uncertainty of $h\nu$.

Lastly, we describe the so-called Fermi-edge correction[88]. Acquisition of a band map while using a straight detection slit on a hemispherical analyzer may result in detection of the photocurrent at shifted $(E^{\mathrm{kin}}, \eta)$. This distortion can be partially corrected with the following steps. First, Fermi-Dirac distributions are fitted for each angle $\eta$, leading to edge estimates $\widehat{h\nu}(\eta) - \widehat{\Phi}(\eta)$. Next, the resulting $\widehat{h\nu}(\eta) - \widehat{\Phi}(\eta)$ are fitted with a polynomial in $\eta$, and a reference angle $\eta^{\mathrm{ref}}$ is assigned for which $\widehat{h\nu}(\eta^{\mathrm{ref}}) - \widehat{\Phi}(\eta^{\mathrm{ref}})$ is assumed to be undistorted. Afterwards, the data at each angle $\eta_j$ with angle index $j$ are shifted according to the difference between the polynomial fit result $\widehat{h\nu}(\eta_j) - \widehat{\Phi}(\eta_j)$ and $\widehat{h\nu}(\eta^{\mathrm{ref}}) - \widehat{\Phi}(\eta^{\mathrm{ref}})$. In xARPES, the edges can be fitted with a polynomial up to second order, while an example with Li-doped graphene is provided in Supplementary Fig. S3.

## Data availability

The raw data of the examples in the Photoemission matrix elements in $TiO_2$-terminated $SrTiO_3$ and Eliashberg function similarity in quasi-freestanding graphene subsections are available in the examples directory of

the xARPES GitHub repository, with further download instructions available in the xARPES documentation. All data for reproducing the figures and the analysis are provided on the Materials Cloud Archive.

## Code availability

The source code of xARPES is available on the GitHub repository, the public version of xARPES can be downloaded from PyPI and Conda Forge, while the documentation is available at Read the Docs.

Received: 4 September 2025; Accepted: 19 February 2026;
Published online: 24 April 2026

## References

1. Bruus, H. & Flensberg, K. *Many-Body Quantum Theory in Condensed Matter Physics: An Introduction* https://doi.org/10.1093/oso/9780198566335.001.0001 (Oxford University Press, 2004).
2. Fröhlich, H. Theory of the superconducting state. I. The ground state at the absolute zero of temperature. *Phys. Rev.* **79**, 845 (1950).
3. Mahan, G. D. *Many-Particle Physics*, 3rd ed edn. https://doi.org/10.1007/978-1-4757-5714-9 (Kluwer Academic/Plenum Publishers, 2000).
4. Coleman, P. *Introduction to Many-Body Physics* 1 edn. https://doi.org/10.1017/CBO9781139020916 (Cambridge University Press, 2015).
5. Allen, P. B. Electron self-energy and generalized Drude formula for infrared conductivity of metals. *Phys. Rev. B* **92**, 054305 (2015).
6. Berthod, C. *Spectroscopic Probes of Quantum Matter* https://iopscience.iop.org/book/mono/978-0-7503-1741-2 (IOP Publishing, 2018).
7. Poncé, S., Margine, E., Verdi, C. & Giustino, F. EPW: electron–phonon coupling, transport and superconducting properties using maximally localized Wannier functions. *Comput. Phys. Commun.* **209**, 116–133 (2016).
8. Allen, P. B. & Mitrović, B. Theory of superconducting $T_c$. *Solid State Phys.* **37**, 1 (1983).
9. Park, J., Zhou, J.-J. & Bernardi, M. Spin-phonon relaxation times in centrosymmetric materials from first principles. *Phys. Rev. B* **101**, 045202 (2020).
10. Franchini, C., Reticcioli, M., Setvín, M. & Diebold, U. Polarons in materials. *Nat. Rev. Mater.* **6**, 560–586 (2021).
11. Yu, T. L. et al. Strong band renormalization and emergent ferromagnetism induced by electron-antiferromagnetic-magnon coupling. *Nat. Commun.* **13**, 6560 (2022).
12. Mazzola, F. et al. Tuneable electron–magnon coupling of ferromagnetic surface states in $PdCoO_2$. *npj Quantum Mater.* **7**, 20 (2022).
13. Lazzari, R., Li, J. & Jupille, J. Dielectric study of the interplay between charge carriers and electron energy losses in reduced titanium dioxide. *Phys. Rev. B* **98**, 075432 (2018).
14. Johnson, P. D. et al. Doping and temperature dependence of the mass enhancement observed in the cuprate $Bi_2Sr_2CaCu_2O_{8+\delta}$. *Phys. Rev. Lett.* **87**, 177007 (2001).
15. Shi, J. et al. Direct extraction of the Eliashberg function for electron-phonon coupling: a case study of Be($10\bar{1}0$). *Phys. Rev. Lett.* **92**, 186401 (2004).
16. Grimvall, G. *The Electron–Phonon Interaction in Metals* (North-Holland, Amsterdam, 1981).
17. Marsiglio, F. & Carbotte, J. P. Electron - Phonon Superconductivity. In Bennemann, K. & Kettterson, J. (eds.) *Superconductivity: Conventional and Unconventional Superconductors*, 73 https://doi.org/10.1007/978-3-540-73253-2_3 (Springer, 2008).
18. Margine, E. R. & Giustino, F. Anisotropic Migdal-Eliashberg theory using Wannier functions. *Phys. Rev. B* **87**, 024505 (2013).
19. Nagamatsu, J., Nakagawa, N., Muranaka, T., Zenitani, Y. & Akimitsu, J. Superconductivity at 39 K in magnesium diboride. *Nature* **410**, 63 (2001).
20. Choi, H. J., Roundy, D., Sun, H., Cohen, M. L. & Louie, S. G. First-principles calculation of the superconducting transition in $MgB_2$ within the anisotropic Eliashberg formalism. *Phys. Rev. B* **66**, 020513 (2002).
21. Marsiglio, F. Inversion of optical conductivity data in metals. *J. Supercond.* **12**, 163–167 (1999).
22. McMillan, W. L. & Rowell, J. M. Lead phonon spectrum calculated from superconducting density of states. *Phys. Rev. Lett.* **14**, 108–112 (1965).
23. Zeljkovic, I. et al. Nanoscale determination of the mass enhancement factor in the lightly doped bulk insulator lead selenide. *Nat. Commun.* **6**, 6559 (2015).
24. Damascelli, A., Hussain, Z. & Shen, Z.-X. Angle-resolved photoemission studies of the cuprate superconductors. *Rev. Mod. Phys.* **75**, 473 (2003).
25. Einstein, A. On a heuristic point of view about the creation and conversion of light. *Ann. Phys.* **17**, 132 (1905).
26. Moser, S. An experimentalist's guide to the matrix element in angle resolved photoemission. *J. Electron Spectrosc. Relat. Phenom.* **214**, 29 (2017).
27. Tusche, C. et al. Spin resolved photoelectron microscopy using a two-dimensional spin-polarizing electron mirror. *Appl. Phys. Lett.* **99**, 032505 (2011).
28. Dil, J. H. Spin- and angle-resolved photoemission on topological materials. *Electron. Struct.* **1**, 023001 (2019).
29. Giustino, F. Electron-phonon interactions from first principles. *Rev. Mod. Phys.* **89**, 015003 (2017).
30. Abrikosov, A. A., Gorkov, L. P., Dzyaloshinski, I. E., Silverman, R. A. & Weiss, G. H. *Methods of Quantum Field Theory in Statistical Physics* https://doi.org/10.1063/1.3051555 (Pergamon Press Ltd., 1964).
31. Veenstra, C. N., Goodvin, G. L., Berciu, M. & Damascelli, A. Spectral function tour of electron-phonon coupling outside the Migdal limit. *Phys. Rev. B* **84**, 085126 (2011).
32. Li, Y. et al. Evidence of strong and mode-selective electron–phonon coupling in the topological superconductor candidate 2M-$WS_2$. *Nat. Commun.* **15**, 6235 (2024).
33. Iwasawa, H. High-resolution angle-resolved photoemission spectroscopy and microscopy. *Electron. Struct.* **2**, 043001 (2020).
34. Chien, T. *Anisotropic electron-phonon coupling on a two-dimensional isotropic Fermi contour: $\bar{\Gamma}$ surface state of Be(0001)*. Ph.D. thesis, University of Tennessee https://trace.tennessee.edu/utk_graddiss/6041/ (2009).
35. Iwasawa, H. et al. High-energy anomaly in the band dispersion of the ruthenate superconductor. *Phys. Rev. Lett.* **109**, 066404 (2012).
36. Cappelli, E. et al. Electronic structure of the highly conductive perovskite oxide $SrMoO_3$. *Phys. Rev. Mater.* **6**, 075002 (2022).
37. Fan, H. Y. Temperature dependence of the energy gap in semiconductors. *Phys. Rev.* **82**, 900 (1951).
38. Migdal, A. B. Interaction between electrons and lattice vibrations in a normal metal. *Sov. Phys. JETP* **7**, 996 (1958).
39. Allen, P. B. & Heine, V. Theory of the temperature dependence of electronic band structures. *J. Phys. C Solid State Phys.* **9**, 2305 (1976).
40. Allen, P. B. & Cardona, M. Theory of the temperature dependence of the direct gap of germanium. *Phys. Rev. B* **23**, 1495 (1981).
41. Marini, A., Poncé, S. & Gonze, X. Many-body perturbation theory approach to the electron-phonon interaction with density-functional theory as a starting point. *Phys. Rev. B* **91**, 224310 (2015).
42. Lafuente-Bartolome, J. et al. Ab Initio self-consistent many-body theory of polarons at all couplings. *Phys. Rev. B* **106**, 075119 (2022).
43. Grimvall, G. The electron-phonon interaction in normal metals. *Phys. Scr.* **14**, 63 (1976).

44. McDougall, B. A., Balasubramanian, T. & Jensen, E. Phonon contribution to quasiparticle lifetimes in Cu measured by angle-resolved photoemission. *Phys. Rev. B* **51**, 13891 (1995).
45. Balasubramanian, T., Jensen, E., Wu, X. L. & Hulbert, S. L. Large value of the electron-phonon coupling parameter ($\lambda = 1.15$) and the possibility of surface superconductivity at the Be(0001) surface. *Phys. Rev. B* **57**, R6866 (1998).
46. Valla, T. et al. Evidence for quantum critical behavior in the optimally doped cuprate $Bi_2Sr_2CaCu_2O_{8+\delta}$. *Science* **285**, 2110 (1999).
47. Jarrell, M. & Gubernatis, J. E. Bayesian inference and the analytic continuation of imaginary-time quantum Monte Carlo data. *Phys. Rep.* **269**, 63 (1996).
48. Chien, T. et al. Electron-phonon coupling in a system with broken symmetry: surface of Be(0001). *Phys. Rev. B* **92**, 075133 (2015).
49. Ludbrook, B. M. *Electron-Phonon Mediated Superconductivity Probed by ARPES: From $MgB_2$ to Lithium-Decorated Graphene*. Ph.D. thesis, The University of British Columbia https://open.library.ubc.ca/soa/clRcle/collections/ubctheses/24/items/1.0135608 (2014).
50. Haberer, D. et al. Anisotropic Eliashberg function and electron-phonon coupling in doped graphene. *Phys. Rev. B* **88**, 081401 (2013).
51. Fedorov, A. V. et al. Observation of a universal donor-dependent vibrational mode in graphene. *Nat. Commun.* **5**, 3257 (2014).
52. Ludbrook, B. M. et al. Evidence for superconductivity in Li-decorated monolayer graphene. *Proc. Natl. Acad. Sci. USA* **112**, 11795 (2015).
53. Verbitskiy, N. I. et al. Environmental control of electron–phonon coupling in barium doped graphene. *2D Mater.* **3**, 045003 (2016).
54. Usachov, D. Y. et al. Electron-phonon coupling in graphene placed between magnetic Li and Si layers on cobalt. *Phys. Rev. B* **97**, 085132 (2018).
55. Ehlen, N. et al. Origin of the flat band in heavily Cs-doped graphene. *ACS Nano* **14**, 1055 (2020).
56. Huempfner, T., Otto, F., Forker, R., Müller, P. & Fritz, T. Superconductivity of K-intercalated epitaxial bilayer graphene. *Adv. Mater. Interfaces* **10**, 2300014 (2023).
57. Zhong, Y. et al. Testing electron–phonon coupling for the superconductivity in kagome metal $CsV_3Sb_5$. *Nat. Commun.* **14**, 1945 (2023).
58. Sokolović, I. et al. Duality and degeneracy lifting in two-dimensional electron liquids on $SrTiO_3$(001). *Nat. Commun.* **16**, 4594 (2025).
59. Røst, H. I. et al. Disentangling electron-boson interactions on the surface of a familiar ferromagnet. *Phys. Rev. B* **109**, 035137 (2024).
60. Bok, J. M. et al. Momentum dependence of the single-particle self-energy and fluctuation spectrum of slightly underdoped $Bi_2Sr_2CaCu_2O_{8+\delta}$ from high-resolution laser angle-resolved photoemission. *Phys. Rev. B* **81**, 174516 (2010).
61. Zhao, L. et al. Quantitative determination of Eliashberg function and evidence of strong electron coupling with multiple phonon modes in heavily overdoped $(Bi,Pb)_2Sr_2CuO_{6+\delta}$. *Phys. Rev. B* **83**, 184515 (2011).
62. Yun, J. H. et al. Analysis of laser angle-resolved photoemission spectra of $Ba_2Sr_2CaCu_2O_{8+\delta}$ in the superconducting state: angle-resolved self-energy and the fluctuation spectrum. *Phys. Rev. B* **84**, 104521 (2011).
63. Marzari, N., Ferretti, A. & Wolverton, C. Electronic-structure methods for materials design. *Nat. Mater.* **20**, 736 (2021).
64. Gonze, X. First-principles responses of solids to atomic displacements and homogeneous electric fields: implementation of a conjugate-gradient algorithm. *Phys. Rev. B* **55**, 10337 (1997).
65. Gonze, X. & Lee, C. Dynamical matrices, Born effective charges, dielectric permittivity tensors, and interatomic force constants from density-functional perturbation theory. *Phys. Rev. B* **55**, 10355 (1997).
66. Baroni, S., de Gironcoli, S., Dal Corso, A. & Giannozzi, P. Phonons and related crystal properties from density-functional perturbation theory. *Rev. Mod. Phys.* **73**, 515 (2001).
67. Poncé, S. et al. Temperature dependence of the electronic structure of semiconductors and insulators. *J. Chem. Phys.* **143**, 102813 (2015).
68. Eiguren, A. & Ambrosch-Draxl, C. Wannier interpolation scheme for phonon-induced potentials: application to bulk $MgB_2$, W, and the (1 × 1) H-covered W(110) surface. *Phys. Rev. B* **78**, 045124 (2008).
69. Gonze, X. et al. The ABINIT project: impact, environment and recent developments. *Comput. Phys. Commun.* **248**, 107042 (2020).
70. Marzari, N., Mostofi, A. A., Yates, J. R., Souza, I. & Vanderbilt, D. Maximally localized Wannier functions: theory and applications. *Rev. Mod. Phys.* **84**, 1419 (2012).
71. Pizzi, G. et al. Wannier90 as a community code: new features and applications. *J. Phys. Condens. Matter* **32**, 165902 (2020).
72. Giustino, F., Cohen, M. L. & Louie, S. G. Electron-phonon interaction using Wannier functions. *Phys. Rev. B* **76**, 165108 (2007).
73. Lee, H. et al. Electron–phonon physics from first principles using the EPW code. *npj Comput. Mater.* **9**, 156 (2023).
74. Gonze, X. et al. Recent developments in the ABINIT software package. *Comput. Phys. Commun.* **205**, 106 (2016).
75. Cepellotti, A., Coulter, J., Johansson, A., Fedorova, N. S. & Kozinsky, B. Phoebe: a high-performance framework for solving phonon and electron Boltzmann transport equations. *J. Phys. Mater.* **5**, 035003 (2022).
76. Zhou, J.-J. et al. PERTURBO: a software package for ab initio electron-phonon interactions, charge transport and ultrafast dynamics. *Comput. Phys. Commun.* **264**, 107970 (2021).
77. Protik, N. H., Li, C., Pruneda, M., Broido, D. & Ordejón, P. The elphbolt ab initio solver for the coupled electron-phonon Boltzmann transport equations. *npj Comput. Mater.* **8**, 28 (2022).
78. Marini, G. et al. EPI*q*: an open-source software for the calculation of electron-phonon interaction related properties. *Comput. Phys. Commun.* **295**, 108950 (2024).
79. Li, Z., Antonius, G., Wu, M., da Jornada, F. H. & Louie, S. G. Electron-phonon coupling from Ab initio linear-response theory within the *GW* method: correlation-enhanced interactions and superconductivity in $Ba_{1-x}K_xBiO_3$. *Phys. Rev. Lett.* **122**, 186402 (2019).
80. Abramovitch, D. J., Zhou, J.-J., Mravlje, J., Georges, A. & Bernardi, M. Combining electron-phonon and dynamical mean-field theory calculations of correlated materials: transport in the correlated metal $Sr_2RuO_4$. *Phys. Rev. Mater.* **7**, 093801 (2023).
81. Matthiessen, A. & Vogt, A. C. IV. On the influence of temperature on the electric conducting-power of alloys. *Philos. Trans. R. Soc. Lond.* **154**, 167 (1864).
82. Kemper, A. F., Abdurazakov, O. & Freericks, J. K. General principles for the nonequilibrium relaxation of populations in quantum materials. *Phys. Rev. X* **8**, 041009 (2018).
83. Kordyuk, A. A. et al. Bare electron dispersion from experiment: self-consistent self-energy analysis of photoemission data. *Phys. Rev. B* **71**, 214513 (2005).
84. Pletikosić, I., Kralj, M., Milun, M. & Pervan, P. Finding the bare band: Electron coupling to two phonon modes in potassium-doped graphene on Ir(111). *Phys. Rev. B* **85**, 155447 (2012).
85. Stansbury, C. & Lanzara, A. PyARPES: an analysis framework for multimodal angle-resolved photoemission spectroscopies. *SoftwareX* **11**, 100472 (2020).
86. Polley, C. M. et al. The Bloch beamline at MAX IV: micro-spot ARPES from a conventional, full-featured beamline. *Synchrotron Radiat. News* **37**, 18 (2024).
87. Bisti, F. NavARP. https://fbisti.gitlab.io/navarp/index.html (2025). Last accessed: 5 July 2025.
88. Han, K. ERLabPy. https://erlabpy.readthedocs.io. (2025). Last accessed: 21 May 2025.

89. Bryan, R. K. Maximum entropy analysis of oversampled data problems. *Eur. Biophys. J.* **18**, 165 (1990).
90. Fero, A., Smallwood, C., Affeldt, G. & Lanzara, A. Impact of work function induced electric fields on laser-based angle-resolved photoemission spectroscopy. *J. Electron Spectros. Relat. Phenom.* **195**, 237 (2014).
91. Ishida, Y. & Shin, S. Functions to map photoelectron distributions in a variety of setups in angle-resolved photoemission spectroscopy. *Rev. Sci. Instrum.* **89**, 043903 (2018).
92. Berglund, C. N. & Spicer, W. E. Photoemission studies of copper and silver: theory. *Phys. Rev.* **136**, A1030 (1964).
93. Schaich, W. L. & Ashcroft, N. W. Model calculations in the theory of photoemission. *Phys. Rev. B* **3**, 2452 (1971).
94. Mahan, G. D. Theory of photoemission in simple metals. *Phys. Rev. B* **2**, 4334 (1970).
95. Keiter, H. Comment on many-body aspects of external photoemission. *Z. Phys. B.* **30**, 167 (1978).
96. Almbladh, C.-O. Photoemission beyond the sudden approximation. *J. Phys. Conf. Ser.* **35**, 127 (2006).
97. Hermeking, H. & Wehrum, R. P. On the derivation of a Golden Rule formula for photoemission in the quadratic response formalism. *J. Phys. C Solid State Phys.* **8**, 3468 (1975).
98. Hüfner, S. *Photoelectron Spectroscopy*, vol. 82 of *Springer Series in Solid-State Sciences* https://doi.org/10.1007/978-3-662-03150-6 (Springer, 1995).
99. Smith, N. V., Thiry, P. & Petroff, Y. Photoemission linewidths and quasiparticle lifetimes. *Phys. Rev. B* **47**, 15476 (1993).
100. Strocov, V. N. et al. High-energy photoemission final states beyond the free-electron approximation. *Nat. Commun.* **14**, 4827 (2023).
101. Iwasawa, H. et al. Development of laser-based scanning $\mu$-ARPES system with ultimate energy and momentum resolutions. *Ultramicroscopy* **182**, 85 (2017).
102. Förster, T., Krüger, P. & Rohlfing, M. *GW* calculations for $Bi_2Te_3$ and $Sb_2Te_3$ thin films: electronic and topological properties. *Phys. Rev. B* **93**, 205442 (2016).
103. Verga, S., Knigavko, A. & Marsiglio, F. Inversion of angle-resolved photoemission measurements in high-$T_c$ cuprates. *Phys. Rev. B* **67**, 054503 (2003).
104. Li, Z., Wu, M., Chan, Y.-H. & Louie, S. G. Unmasking the origin of kinks in the photoemission spectra of cuprate superconductors. *Phys. Rev. Lett.* **126**, 146401 (2021).
105. Chubukov, A. V. & Maslov, D. L. First-Matsubara-frequency rule in a Fermi liquid. I. Fermionic self-energy. *Phys. Rev. B* **86**, 155136 (2012).
106. Allen, P. B. Solids with thermal or static disorder. I. One-electron properties. *Phys. Rev. B* **18**, 5217 (1978).
107. Allen, P. B. & Silberglitt, R. Some effects of phonon dynamics on electron lifetime, mass renormalization, and superconducting transition temperature. *Phys. Rev. B* **9**, 4733 (1974).
108. Eiguren, A., Ambrosch-Draxl, C. & Echenique, P. M. Self-consistently renormalized quasiparticles under the electron-phonon interaction. *Phys. Rev. B* **79**, 245103 (2009).
109. Wen, C. H. P. et al. Unveiling the superconducting mechanism of $Ba_{0.51}K_{0.49}$ $BiO_3$. *Phys. Rev. Lett.* **121**, 117002 (2018).
110. Rudin, S. P., Bauer, R., Liu, A. Y. & Freericks, J. K. Reevaluating electron-phonon coupling strengths: indium as a test case for ab initio and many-body theory methods. *Phys. Rev. B* **58**, 14511 (1998).
111. Gull, S. F. Developments in maximum entropy data analysis. In Skilling, J. (ed.) *Developments in Maximum Entropy Data Analysis*, Maximum Entropy and Bayesian Methods, 53–71 https://doi.org/10.1007/978-94-015-7860-8_4 (Springer, 1989).
112. Kaufmann, J. & Held, K. Ana_cont: Python package for analytic continuation. *Comput. Phys. Commun.* **282**, 108519 (2023).
113. Levy, G., Nettke, W., Ludbrook, B. M., Veenstra, C. N. & Damascelli, A. Deconstruction of resolution effects in angle-resolved photoemission. *Phys. Rev. B* **90**, 045150 (2014).
114. Plumb, N. C. et al. Low-Energy (<10 meV) feature in the nodal electron self-energy and strong temperature dependence of the Fermi velocity in $Bi_2Sr_2CaCu_2O_{8+\delta}$. Phys. Rev. Lett. 105, 046402 (2010).
115. Jiang, J. et al. High-resolution angle-resolved photoemission study of the Al(100) single crystal. *e-J. Surf. Sci. Nanotechnol.* **7**, 57 (2009).
116. Zhou, X. J. et al. Multiple bosonic mode coupling in the electron self-energy of $(La_{2-x}Sr_x)CuO_4$. *Phys. Rev. Lett.* **95**, 117001 (2005).
117. King, P. D. C. et al. Quasiparticle dynamics and spin–orbital texture of the $SrTiO_3$ two-dimensional electron gas. *Nat. Commun.* **5**, 3414 (2014).
118. Day, R. P., Zwartsenberg, B., Elfimov, I. S. & Damascelli, A. Computational framework Chinook for angle-resolved photoemission spectroscopy. *npj Quantum Mater.* **4**, 54 (2019).
119. Schüler, M. et al. Polarization-modulated angle-resolved photoemission spectroscopy: toward circular dichroism without circular photons and Bloch wave-function reconstruction. *Phys. Rev. X* **12**, 011019 (2022).
120. Kern, C. S. et al. Simple extension of the plane-wave final state in photoemission: Bringing understanding to the photon-energy dependence of two-dimensional materials. *Phys. Rev. Res.* **5**, 033075 (2023).
121. Ryoo, J. H. & Park, C.-H. Lippmann-Schwinger approach for accurate photoelectron wave functions and angle-resolved photoemission spectra from first principles. *Phys. Rev. Lett.* **135**, 056403 (2025).
122. Ebert, H., Ködderitzsch, D. & Minár, J. Calculating condensed matter properties using the KKR-Green's function method—recent developments and applications. *Rep. Prog. Phys.* **74**, 096501 (2011).
123. Zhou, J.-J., Hellman, O. & Bernardi, M. Electron-phonon scattering in the presence of soft modes and electron mobility in $SrTiO_3$ Perovskite from First Principles. *Phys. Rev. Lett.* **121**, 226603 (2018).
124. Zhou, J.-J. & Bernardi, M. Predicting charge transport in the presence of polarons: The beyond-quasiparticle regime in $SrTiO_3$. *Phys. Rev. Res.* **1**, 033138 (2019).
125. Chen, C., Avila, J., Frantzeskakis, E., Levy, A. & Asensio, M. C. Observation of a two-dimensional liquid of Fröhlich polarons at the bare $SrTiO_3$ surface. *Nat. Commun.* **6**, 8585 (2015).
126. Wang, Z. et al. Tailoring the nature and strength of electron–phonon interactions in the $SrTiO_3$(001) 2D electron liquid. *Nat. Mater.* **15**, 6 (2016).
127. Guedes, E. B. et al. Single spin-polarized Fermi surface in $SrTiO_3$ thin films. *Phys. Rev. Res.* **2**, 033173 (2020).
128. Faeth, B. D. et al. Interfacial electron-phonon coupling constants extracted from intrinsic replica bands in monolayer FeSe/$SrTiO_3$. *Phys. Rev. Lett.* **127**, 016803 (2021).
129. Goldberg, S., Fadley, C. & Kono, S. Photoionization cross-sections for atomic orbitals with random and fixed spatial orientation. *J. Electron Spectrosc. Relat. Phenom.* **21**, 285 (1981).
130. Vogt, H. Hyper-Raman tensors of the zone-center optical phonons in $SrTiO_3$ and $KTaO_3$. *Phys. Rev. B* **38**, 5699 (1988).
131. Zhou, X. et al. New developments in laser-based photoemission spectroscopy and its scientific applications: a key issues review. *Rep. Prog. Phys.* **81**, 062101 (2018).
132. Cancellieri, C. et al. Polaronic metal state at the $LaAlO_3$/$SrTiO_3$ interface. *Nat. Commun.* **7**, 10386 (2016).
133. Alarab, F. et al. Nature of the metallic and in-gap states in Ni-doped $SrTiO_3$. *APL Mater.* **12**, 011118 (2024).
134. Santander-Syro, A. F. et al. Giant spin splitting of the two-dimensional electron gas at the surface of $SrTiO_3$. *Nat. Mater.* **13**, 1085 (2014).

135. Fabian, J. & Das Sarma, S. Phonon-induced spin relaxation of conduction electrons in aluminum. *Phys. Rev. Lett.* **83**, 1211 (1999).
136. Hwang, J., Timusk, T., Schachinger, E. & Carbotte, J. P. Evolution of the bosonic spectral density of the high-temperature superconductor $Bi_2Sr_2CaCu_2O_{8+\delta}$. *Phys. Rev. B* **75**, 144508 (2007).
137. Zhang, H. et al. Angle-resolved photoemission spectroscopy. *Nat. Rev. Methods Primers* **2**, 54 (2022).
138. Poncé, S., Royo, M., Stengel, M., Marzari, N. & Gibertini, M. Long-range electrostatic contribution to electron-phonon couplings and mobilities of two-dimensional and bulk materials. *Phys. Rev. B* **107**, 155424 (2023).
139. Margine, E. R. & Giustino, F. Two-gap superconductivity in heavily *n*-doped graphene: *Ab initio* Migdal-Eliashberg theory. *Phys. Rev. B* **90**, 014518 (2014).
140. Novko, D. Dopant-induced plasmon decay in graphene. *Nano Lett.* **17**, 6991 (2017).
141. Hwang, E. H. & Das Sarma, S. Quasiparticle spectral function in doped graphene: Electron-electron interaction effects in ARPES. *Phys. Rev. B* **77**, 081412 (2008).
142. Park, C.-H., Giustino, F., Spataru, C. D., Cohen, M. L. & Louie, S. G. First-principles study of electron linewidths in graphene. *Phys. Rev. Lett.* **102**, 076803 (2009).
143. Grüneis, A. et al. Electronic structure and electron-phonon coupling of doped graphene layers in $KC_8$. *Phys. Rev. B* **79**, 205106 (2009).
144. Tang, S.-J. et al. A spectroscopic view of electron–phonon coupling at metal surfaces. *Phys. Status Solidi (b)* **241**, 2345 (2004).
145. Fajardo, E. A. & Winkler, R. Effective dynamics of two-dimensional Bloch electrons in external fields derived from symmetry. *Phys. Rev. B* **100**, 125301 (2019).
146. Romero, A. H. et al. ABINIT: overview and focus on selected capabilities. *J. Chem. Phys.* **152**, 124102 (2020).
147. Jiang, J. et al. Coupling parameters of many-body interactions for the Al(100) surface state: a high-resolution angle-resolved photoemission spectroscopy study. *Phys. Rev. B* **84**, 155124 (2011).
148. Lihm, J.-M. & Poncé, S. Nonperturbative self-consistent electron-phonon spectral functions and transport. *Phys. Rev. Lett.* **134**, 186401 (2025).
149. Aryasetiawan, F., Hedin, L. & Karlsson, K. Multiple plasmon satellites in Na and Al spectral functions from Ab initio cumulant expansion. *Phys. Rev. Lett.* **77**, 2268 (1996).
150. Varma, C. M., Littlewood, P. B., Schmitt-Rink, S., Abrahams, E. & Ruckenstein, A. E. Phenomenology of the normal state of Cu-O high-temperature superconductors. *Phys. Rev. Lett.* **63**, 1996 (1989).
151. Bostwick, A., Ohta, T., Seyller, T., Horn, K. & Rotenberg, E. Quasiparticle dynamics in graphene. *Nat. Phys.* **3**, 36 (2007).
152. LMFIT developers. LMFIT. https://lmfit.github.io/lmfit-py/index.html. (2025). Last accessed: 5 July 2025.
153. Virtanen, P. et al. SciPy 1.0: fundamental algorithms for scientific computing in Python. *Nat. Methods* **17**, 261 (2020).
154. Hellbrück, L. et al. High-resolution MHz time- and angle-resolved photoemission spectroscopy based on a tunable vacuum ultraviolet source. *Rev. Sci. Instrum.* **95**, 033007 (2024).


## Acknowledgements

We gratefully acknowledge the data for Li-doped graphene shared by Dmitry Yu. Usachov and Denis V. Vyalikh[54], as well as the $SrTiO_3$ data shared by Igor Sokolović (not previously published), and the Al(100) data provided by Kenya Shimada[147]. The authors would like to thank Eduardo Bonini Guedes, TeYu Chien, Kenya Shimada, Dmitry Yu. Usachov, Simon Moser, Cheol-Hwan Park, Jae-Mo Lihm, and Feliciano Giustino for useful discussions. T.P.v.W. is a Research Fellow of the F.R.S. -FNRS. S.P. is a Research Associate of the Fonds de la Recherche Scientifique - FNRS. This publication was supported by the Walloon Region in the strategic axis FRFS-WEL-T. J.B. and N.M. acknowledge funding by the Deutsche Forschungsgemeinschaft (DFG, German Research Foundation) under Germany's Excellence Strategy (University Allowance, EXC 2077, University of Bremen). N.M. acknowledges support by the NCCR MARVEL, a National Centre of Competence in Research, funded by the Swiss National Science Foundation (grant number 205602). Computational resources have been provided by the EuroHPC JU award granting access to MareNostrum5 at Barcelona Supercomputing Center (BSC), Spain (Project ID: EHPC-EXT-2023E02-050), and by the Consortium des Équipements de Calcul Intensif (CÉCI), funded by the FRS-FNRS under Grant No. 2.5020.11 and computational resources on Lucia, the Tier-1 supercomputer of the Walloon Region with infrastructure funded by the Walloon Region under the grant agreement n°1910247.

## Author contributions

T.P.v.W. wrote the first draft with contributions from C.B.; T.P.v.W. wrote the code with contributions from J.B.; S.P., J.H.D., and N.M. conceived and supervised the project. All authors reviewed and approved the final version of the manuscript.

## Competing interests

The authors declare no competing interests.

## Additional information

**Supplementary information** The online version contains supplementary material available at https://doi.org/10.1038/s41524-026-02026-9.

**Correspondence** and requests for materials should be addressed to Thomas P. van Waas or Samuel Poncé.